

Detection and analysis of Lhù'ään Mân' (Kluane Lake) dust plumes using passive and active ground-based remote sensing supported by physical surface measurements

Seyed Ali Sayedain¹, Norman T. O'Neill¹, James King², Patrick L. Hayes², Daniel Bellamy², Richard Washington³, Sebastian Engelstaedter³, Andy Vicente-Luis², Jill Bachelder², Malo Bernhard²

¹Centre d'Applications et de Recherches en Télédétection, Université de Sherbrooke, Sherbrooke, Canada

²Université de Montréal, Montréal, Canada

³University of Oxford, Oxford, United Kingdom

Correspondence to: S. A. Sayedain (seyed.ali.sayedain@usherbrooke.ca)

Abstract. There is growing recognition that high latitude dust (HLD), originating from local, drainage-basin flows, is the dominant source for certain important phenomena such as particle deposition on snow / ice. The analysis of such local plumes (including a better exploitation of remote sensing data) has been targeted as a key aerosol issue by the HLD community. The sub-Arctic Lhù'ään Mân' (Kluane Lake) region in the Canadian Yukon is subject to regular drainage, wind-induced dust plumes. This dust emission site is one of many current and potential proglacial dust sources in the Canadian North. In situ ground-based measurements are, due to constraints in accessing these types of regions, rare. Ground- and satellite-based remote sensing accordingly play an important role in helping characterize local dust sources in the Arctic and sub-Arctic.

We compared ground-based, passive and active remote sensing springtime (May 2019) retrievals with microphysical surface-based measurements in the Lhù'ään Mân' region in order to better understand the potential for ground- and satellite-based remote sensing of HLD plumes. This included correlation analyzes between ground-based coarse mode (CM) aerosol optical depth (AOD) retrievals from AERONET AOD spectra, CM AODs derived from co-located Doppler lidar profiles and OPS (Optical Particle Sizer) surface measurements of CM particle-volume concentration ($v_c(0)$). An automated dust classification scheme was developed to objectively identify local dust events. The classification process helped distinguish lidar-derived CM AODs which co-varied with $v_{dust}(0)$ (during recognized dust events) and those that varied at the same columnar scale as AERONET-derived CM AOD (and thus could be remotely sensed). False positive cloud events for which dust-induced, high frequency variations in lidar-derived CM AODs in cloudless atmospheres indicated that the AERONET cloud-screening process was rejecting CM dust AODs. The persistence of a positive lidar ratio bias in comparing the CIMEL/lidar-derived value with a prescribed value obtained from OPS-derived particle sizes coupled with dust-speciation-derived refractive indices led to the suggestion that the prescribed value could be increased to optically-derived values of 20 sr by the presence of optically significant dust particles at an effective radius of 11–12 μm . Bimodal CM PSDs from full-fledged AERONET inversions (the combination of AOD spectra and almucantar radiances) also showed CM peaks at $\sim 1.3 \mu\text{m}$ and 5–6.6 μm radius: this, we argued, was associated with springtime Asian dust and Lhù'ään Mân' dust, respectively.

Correlations between the CIMEL-derived fine mode (FM) AOD and FM OPS-derived particle-volume concentration suggest that remote sensing techniques can be employed to monitor FM dust (which is arguably a better indicator of the long-distance transport of HLD).

35 **1 Introduction**

Local, drainage wind-induced dust events have recently been recognized as an important source of dust at high latitudes (Bullard et al., 2016). Groot-Zwaafink et al. (2016) employed FLEXPART simulations to argue that the contributions of Asian, African, and local dust in the Arctic are roughly evenly divided in terms of total atmospheric (columnar) dust loads while surface concentrations are significantly more associated with dust of local origin. Meinander et al. (2022) employed two
40 global dust-transport models supported by recent verification data to confirm the predominance of high latitude dust (HLD) sources in terms of snow- and ice-deposition. This means, notably that, dust deposition on snow and ice and the attendant effects or early snow melt is largely attributable to local dust. Additional impacts of local dust deposition include direct addition of nutrients, local health impacts for humans & wildlife and indirect climate / radiative (altered cloud property) impacts (Meinander et al., 2022). These substantive impacts underscore the importance of understanding the dynamics of local dust
45 transport and deposition.

Bullard et al. (2016) pointed out that local dust events in Canada are rarely monitored compared with other high-latitude countries. Low population density, limited numbers of meteorological stations, and problems with the use of satellite-based remote sensing (RS) data in high-latitude regions (e.g., cloud contamination) have led to less frequent observations of local dust events in Canada (Bullard et al., 2016). The next generation of active and passive polar-orbiting sensors targeted by the
50 ESA EarthCARE mission and the NASA-led Atmospheric Observation System (AOS) promise a quality of aerosol, cloud and precipitation retrievals that will make significant instrumental, algorithmic and scientific advances relative to the polar-orbiting A-train constellation (the workhorse remote sensing constellation that has driven atmospheric science over the past twenty two years). An intrinsic part of that system will be the ground-based Cal/Val sites that employ or will employ active and passive ground-based remote sensing sensors as well as microphysical measurements to monitor aerosols and clouds at existing and
55 future sites across the Arctic. The Lhù'ààn Mân'¹ (Kluane Lake) region of Yukon, Canada will very likely be such a Cal/Val site in the HLD context: it is recognized for its frequent and strong springtime dust events induced by strong katabatic winds, highly erodible sediments and the steep valley walls leading down to the lake (Bachelder et al., 2020).

Published results on the remote sensing of local dust in the Arctic using active or passive, airborne- or satellite-based platforms are rare. Specific examples include the use of airborne (532 nm) lidar profiles to detect local dust plumes over
60 riverbed, fjord and coastal regions of Svalbard (Dörnbrack et al., 2010), MODIS-based color and AOD (aerosol optical depth)

¹ Lhù'ààn Mân' is the Southern Tutchone name for Kluane Lake. Southern Tutchone is one of seven Athapaskan languages in the Yukon and is spoken by Kluane First Nation people.

imagery for dust plumes emanating from Alaskan riverbed sediments into the Gulf of Alaska (Crusius et al., 2011), the investigations by Dagsson-Waldhauserova et al. (2019) who employed MODIS color imagery and attempted to use satellite-based CALIOP lidar profiles to support their airborne particle size distribution measurements of Icelandic dust plumes and MODIS, MISR, CloudSat / CALIOP optical depth and particle size characterization of local dust plumes over Lake Hazen in the high Canadian Arctic (Ranjbar et al., 2021). More recently, Kawai et al. (2023) reported on a multi-year CALIOP-derived climatology of zonally-averaged estimates of local dust optical depth in the Arctic (as well as a unique, multi-year, simulated, map of local-dust columnar concentration across the Arctic)

Ground-based data retrievals using solar extinction and sky radiometry data are widely used by the AERONET (AERosol ROBotic NETwork) to characterize the optical and microphysical properties of aerosols at local (site-focused) scales (Holben et al., 1998). AOD and almucantar sky radiance measurements are carried out using the CIMEL sunphotometer / sky radiometer. Spectral Deconvolution Algorithm (SDA) retrievals can be employed to investigate high frequency event-level studies (O'Neill et al., 2003) while the more comprehensive AERONET inversion algorithm (Dubovik & King, 2000) can be employed for low frequency, climatological-scale analysis (see Hesaraki et al., 2017 for a more detailed discussion). Publications on the use of AERONET retrievals and/or ground-based lidar data to characterize the properties of local dust events at high latitudes are also rare. Yang et al. (2020) employed AERONET AODs and AERONET-derived particle size distributions, surface particle concentration measurements (PM_{2.5} and PM₁₀) as well as Doppler lidar profiles (including the use of a particle-typing depolarization-ratio channel) and ceilometer profiles to characterize the dynamics of local dust events over Iceland. Rozwadowska & Sobolewski (2010), while acknowledging the episodic optical importance of local dust storms such as those detected by Dörnbrack et al. (2010), present a long-range transport and local meteorology analysis of AERONET AODs at Hornsund: an analysis that implies that local dust is of secondary optical importance (at least in the context of total AOD: they did not pursue the analysis in terms of the possible impact of the local meteorology on their coarse mode² (CM) AOD.³)

Huck et al. (2023) employed meteorological measurements, along with AERONET AODs and Angstrom exponents (AOD spectral information), a remote camera and satellite imagery to investigate dust event detection limits in the Lhù'ààn Mân' region. One notable conclusion was that the oblique camera captured many dust blowing incidents that were not being detected by their AERONET CIMEL instrument. Various explanations for this discrepancy were offered: these included 1) the notion that Lhù'ààn Mân' plumes are very locally inhomogeneous and that wind direction could influence AERONET dust detection, that 2) the CIMEL instrument missed plumes below its minimum angular elevation, that 3) AERONET sensitivity was frequently too coarse to detect weaker events, that 4) AERONET cloud screening removed 97.8% of dust events and that 5)

² particles whose radius is microphysically or (in an indirect fashion) optically $> \sim 1 \mu\text{m}$ (see, for example, O'Neill et al., 2022)

³ The AERONET CM AOD product being, on average, significantly less than the total AOD (AboEl-Fetouh et al., 2020) and, in principle, much more sensitive to local CM aerosols such as sea salt and local dust.

90 the CIMEL employed for the analysis (for which data acquisition occurred during the 2018 dust season) was incapable of making nighttime measurements.

Ground-based (and, even more so, satellite-based) remote sensing methods suffer from and benefit from their relatively coarse, column-based spatial scale and their minute to hourly to daily temporal scale. Columnar methods integrate the aerosol effects of the whole column and rely on other dimensions of information to separate out the optical influence of low altitude
95 dust plumes. This same coarseness can have the tendency to produce robust dust signals if the dust plume scale is commensurate with the remote sensing scale. Another challenge related specifically to ground-based and specifically AERONET retrievals is the excessively aggressive cloud screening that can screen out a dust event (Evan et al., 2021) and secondly, insufficiently aggressive cloud screening that leaves residual cloud OD to contaminate potential dust signals. Surface microphysical measurements such as PSDs and vertical profiling measurements such as lidar backscatter profiles can help to
100 verify that dust events are predominantly coarse mode in nature.

We seek to employ ground-based, passive and active (lidar) RS techniques to analyze the complementarity and redundancy of optical and microphysical retrievals relative to springtime CM measurements of local dust acquired using microphysical instruments at Lhù'ààn Mân'. The key ground-based instruments include a CIMEL sunphotometer / sky radiometer, a Doppler lidar operating in the SWIR (short-wave infrared), and an Optical Particle Sizer (OPS) for the measurement of near-surface
105 particle-volume size distributions (PSDs). The coherencies and incoherencies between the passive AERONET retrievals and near-surface PSDs, between AERONET CM AODs and the lidar backscatter profiles and their derived CM AODs (largely generated by CM particle backscatter for the Doppler SWIR lidar) and between the lidar profiles and the CM portion of the near-surface PSDs will enable a better understanding of the optical and microphysical properties of local dust plumes and will help in improving ground-based and satellite-based remote sensing retrievals of local dust properties.

110 **2 Research site and instrumentation**

The Lhù'ààn Mân' region in the Canadian Yukon is subject to regular drainage-wind dust plumes emanating from the Slims River basin (Nickling, 1978). The recent Kaskawulsh glacier retreat in the Slims River Valley and the river reorganization event (Shugar et al., 2017) prompted the fall of water levels and the season-long exposure of the river delta and floodplain. This caused extended periods of dust emissions induced by Aeolian erosion (Shugar et al., 2017). Typically, the
115 period of the most intense dust events is the spring and summer of each year (Bachelder et al., 2020).

The Kluane Lake Research Station (KLRS) is an established University of Calgary (Atmospheric Institute of North America) site on the southern shore of Lhù'ààn Mân' (see Fig. 1). The AERONET CIMEL, Doppler lidar and OPS data employed in this paper were acquired at KLRS during the month of May 2019. The May 2019 campaign was an intense part of a continuous strategy to extract and analyze Lhù'ààn Mân' dust plume properties using a suite of optical, microphysical,

120 and meteorological instruments (a major chemical and microphysical contribution to this ongoing analysis was reported in Bachelder et al., 2020).

Details on the CIMEL sunphotometer / sky radiometer and associated processing protocols can be found in Giles et al. (2019). AEROCAN, the Canadian subnetwork of AERONET (maintained by Environment and Climate Change Canada) provides direct instrument troubleshooting and swapping out support for all Canadian AERONET sites. This instrument
125 provides spectral AOD retrievals at a nominal high frequency of one (9-band) AOD spectrum per 3 minutes (9 bands from 340 to 1640 nm⁴). It also provides a comprehensive suite of low frequency (nominally once per hour) microphysical and optical retrievals derived from almucantar radiance scans and 4-band AODs.

The high frequency (11-second time bin) Doppler (HALO Photonics) lidar (Pearson et al., 2009) was averaged to the 1-minute CIMEL time bins. The vertical resolution of the lidar is 3 m based on 30 m overlapping gates with a typical range of <
130 LCH (Lidar Ceiling Height which is equal to 9.6 km; Newsom & Krishnamurthy, 2020). Its 1.5 μm wavelength (more precisely 1.548 μm according to Newsom & Krishnamurthy, 2020) is largely the result of a strategic decision to minimize molecular contributions to the backscatter signal (see, Newsom & Krishnamurthy, 2020, for example). The FM⁵ AOD at the lidar wavelength is typically negligible (see below).

The KLRS surface-PSD device is a TSI Optical Particle Sizer (OPS) 3330 instrument that incorporates 16 size bins with
135 bin-center radii extending from 0.17 to 4.51 μm (bin-center diameters from 0.34 to 9.02 μm). Two supporting FAI Optical Particle Counter (OPC) instruments provided analogous PSD measurements⁶ at the Down Valley (DV) site about 7 km southwest of KLRS (see Fig. 1 for the DV position and Bachelder et al., 2020 for details on the OPC instruments). The KLRS OPS and the two DV OPC instruments often provided important redundancy information (as well as insightful information stemming from their differences) when we sought to investigate the presence and nature of a given CM event.

140 A dust event captured in a 27 May 2019 PlanetScope satellite image acquired over Lhù'ààn Mân' is shown in Fig. 1 (the KLRS and DV site positions are indicated by red and green stars respectively). AERONET CM AOD retrievals are represented by the blue-colored profile in the bottom right-hand corner of the image. The time of the PlanetScope image acquisition is indicated by the arrow on the AERONET plot. The sun-pointing CIMEL instrument was looking southeast at the time of the PlanetScope image acquisition while dust plumes can be seen flowing from the whitish Slims River basin and delta. The blue-
145 colored AERONET CM AOD shows quite large values during the period (late morning to early afternoon) when the optically significant dust plume intercepts the CIMEL line of sight (from the roughly eastern to western directions).

⁴ Including two bands at 1020 nm that are associated with the overlap region of the two CIMEL detectors (the VIS–NIR and NIR–SWIR detectors).

⁵ particles whose radius is microphysically or (in an indirect fashion) optically $< \sim 1 \mu\text{m}$ (O'Neill et al., 2022)

⁶ across 22 size bins whose bin-center radii extend from 0.14 to 5.0 μm (bin-center diameters from 0.28 to 10 μm)

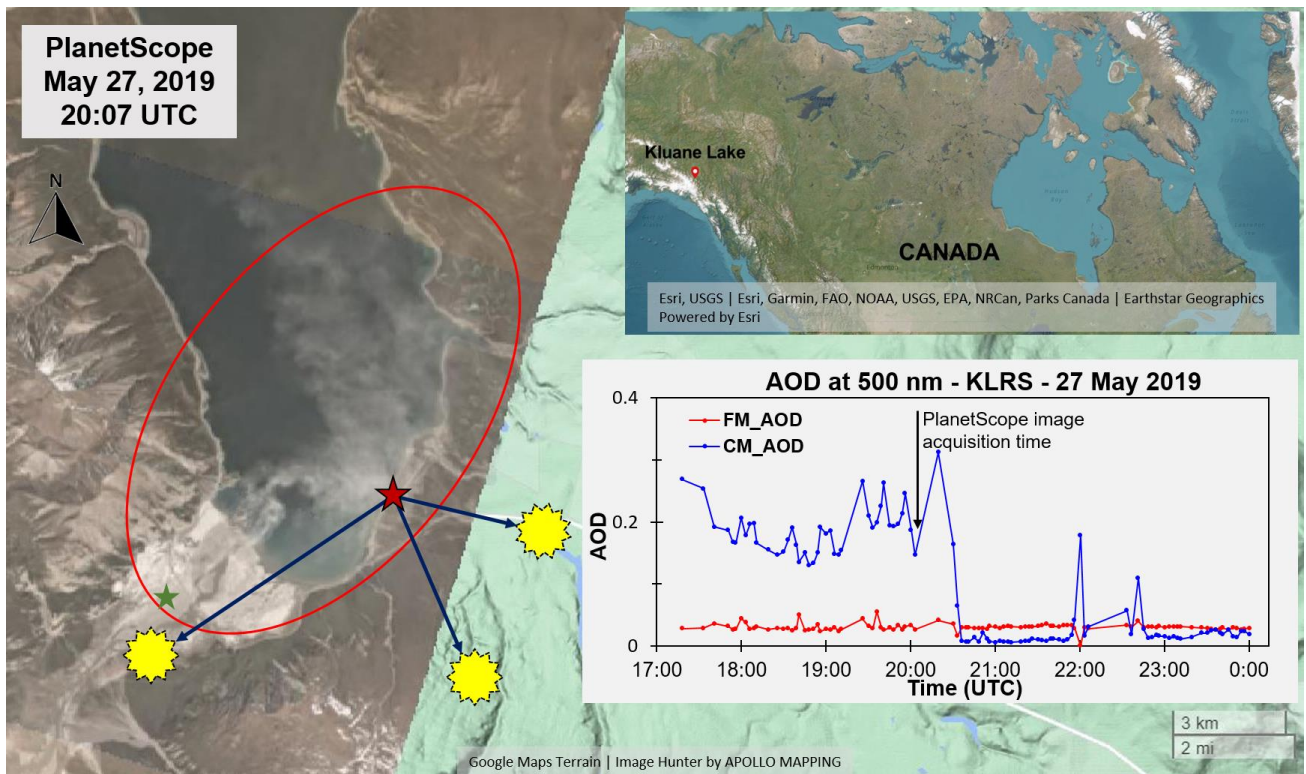


Figure 1: Lhù'ään Mân' (Kluane Lake) study area as seen in a 27 May 2019 PlanetScope satellite image (ESA/NASA). A dust plume can be seen emanating from the whitish Slims River basin. The KLRS and DV site positions are indicated by the red and green star respectively. The CM AOD and FM AOD time series in the bottom right-hand corner is a standard (SDA) AERONET Version 3, Level 1.0 (500 nm) product (the CM AOD at the lidar wavelength of 1.548 μm will only change by a moderate amount relative to the 500 nm value). The solar-viewing azimuth direction of the CIMEL is shown yellow solar icons (clockwise from 17:00 UTC at the upper right to 20:07 UTC to 00:00 UTC on May 28). The coordinates of the AERONET / AEROCAN station are 61.027° N, 138.41° W.

3 Methodology

155 3.1 AERONET processing

We employed Version 3.0 Level 1.0 AODs and Level 1.5 AERONET inversions to extract retrieval products that could be compared with the lidar and the KLRs OPS data sets (see Giles et al., 2019 for an overview of Version 3.0 AERONET AOD products and Sinyuk et al., 2020 for an overview of Version 3 AERONET inversions). The algorithm used for comparisons with the Doppler lidar data was the high frequency (nominally 1 minute averaging bin, 3 minute intersample gap) SDA⁺ product extrapolated to the Doppler SWIR wavelength of 1.548 μm (see O'Neill et al., 2008 for a discussion of the SDA⁺ algorithm). We label this AERONET-derived CM AODs as τ_c .

The low frequency (nominally 1-hour intersample gap) AERONET inversion products (Dubovik & King, 2000) include the particle-volume PSD per unit increment in $\log_r (dV/d\ln r)$ over 22 radius bin centers (stretching from 0.05 to 15 μm) along

with pan-PSD refractive index, scattering phase function and associated optical products such as the asymmetry factor across
 165 four spectral bands (440, 675, 870, and 1020 nm). These fundamental products are accompanied by derived products of CM
 and FM particle-volume concentration and effective radius as well as CM and FM AODs across the same four spectral bands.

An important intensive (per particle) AERONET inversion product is the (column averaged) CM effective radius (see
 Hansen & Travis, 1974 for a definition of the effective radius and AboEl-Fetouh et al., 2020 for a discussion of the FM and
 CM AERONET-inversion effective radius product). In the absence of clouds and in the presence of a strong columnar dust
 170 activity, this parameter may provide an important and robust indicator of column-averaged effective radius. The same can be
 said of the refractive index product with two notable riders: the pan-PSD nature of the product can become problematic in the
 presence of an (optically) competitive FM aerosol of distinctly different refractive index and the rapidly increasing refractive
 index and single scattering albedo retrieval errors (notably for desert dust) with decreasing AOD (Sinyuk et al., 2020).

3.2 Lidar processing

175 Basic lidar definitions are given, for example, in Weitkamp (2005). The essential quantities that we require in order to
 transform the Doppler lidar profiles into CM extinction coefficient and lidar-derived CM optical depth (τ_c^l) are the CM
 backscatter coefficient (β_c) and the CM lidar ratio (S_c). The actual lidar outputs are $\beta'(z) = \beta(z) T^2(z)$ (attenuated
 backscatter coefficient) profiles where $T^2(z)$ is the altitude (z) dependent return (two-way) transmission of a lidar pulse from
 the ground ($z = 0$). Optical depths for submicron particles at the lidar SWIR wavelength are negligible (we already know that
 180 to be true for molecular scattering and it is generally a good approximation if dust optical depths are $>\sim 0.1$: see, for example,
 Fig. 2 of O'Neill et al., 2008⁷).

If we apply this CM dominance to the $\beta'(z)$ and $\beta(z)$ profiles then;

$$\beta'(z) \cong \beta'_c(z) = \beta_c(z) T_c^2(z) \quad (1a)$$

The two-way transmission can be approximated by;

$$185 \quad T_{c,\sim}^2(z) \cong \exp[-2 \tau_c(\tau_{\beta'_c}(0, z)/\tau_{\beta'_c})] \quad (1b)$$

where τ_c is a CIMEL-derived value at the lidar wavelength (τ_c values interpolated to the nominal time of a given lidar
 profile) and $\tau_{\beta'_c}(0, z)/\tau_{\beta'_c}$ amounts to a dynamic approximation of $\tau_c(0, z)/\tau_c$ for that profile (the reader will note that, for the
 sake of nomenclature simplicity, we only employ the partial column argument “(0, z)” when it helps to underscore an explicit
 point). We can then approximate $\beta_c(z)$ by:

$$190 \quad \beta_{c,\sim}(z) \cong \beta'_c(z)/T_{c,\sim}^2(z) \cong \beta_c(z) T^2(z)/T_{c,\sim}^2(z) \quad (2)$$

⁷ For FM AODs of $<\sim 0.4$ at 500 nm (a maximum FM AOD of 0.4 is generally greater than any values that could be found, in
 the absence of the easily detectible influence of biomass burning smoke, at Lhù'àn Mân'). During the month of May 2019
 there were FM AOD events on May 7/8 and May 24 (associated, it would appear with CM dust events) for which the 500 nm
 FM AOD for the former case was as large as ~ 0.2).

The division by $T_{c,\sim}^2(z)$ means (whether it is an approximation or not) that the derived $\beta_c(z)$ values will appear progressively brighter than $\beta'_c(z)$ values as z increases with an attendant potential for error as $T^2(z)$ and $T_{c,\sim}^2(z)$ become very small. However, the $T_{c,\sim}^2(z)$ values are increasingly pinioned (in addition to the near-surface restraint of near unity transmission) by the CIMEL-estimated true value ($\exp[-2\tau_c]$) as z increases towards the upper extreme of the
 195 $\beta'_c(z)$ integration (top of a dust plume in the case of a clear-sky dust event).

3.2.1 Prescribed lidar ratio for dust

A prescribed KLRS-derived lidar ratio⁸ for dust (S_c^p ; results presented below) and a prescribed lidar ratio for cloud (Chiang et al., 2002) were employed to calculate τ_c^ℓ for dust and cloud. If τ_{β_c} is defined as $\int \beta_{c,\sim}(z) dz$ then;

$$\tau_c^\ell \cong S_c^p \tau_{\beta_c} \quad (3)$$

200 S_c^p can be computed from a priori or measurement information on refractive index, particle size and particle shape. We discuss below (Sect. 4.3.1.2) how the prescribed KLRS-derived S_c^p value for dust was arrived at and how much uncertainty was associated with that value.

3.2.2 Validation of prescribed lidar ratio

CIMEL values of τ_c were employed to validate the prescribed dust lidar ratio (effectively the replacement of τ_c^ℓ by τ_c in
 205 Eq. (3) above). Details of the validation parameterization are given in Appendix A1. The process explicitly incorporates S_c^p and τ_c^ℓ and CIMEL-derived τ_c values to compute a CIMEL-referenced lidar ratio (S_c). It includes an accounting of the day-to-day correlations between τ_c^ℓ and τ_c (which may or may not be strong during any given period of interest) and how those correlation results should be weighted.

3.3 OPS and OPC processing

210 The KLRS OPS and the DV OPC PSD measurements of $dn/d\log D$ (particle number / unit volume of air / unit increment in logarithmic diameter) were converted to $dv/d\log D$ (particle-volume / unit volume of air / unit increment in logarithmic diameter) assuming spherical particles⁹. We integrated the OPS PSDs over the CM radius range (bin-centers of 0.78 to 4.51 μm) to yield the CM particle-volume concentration ($v_c(0)$: the volume of all CM particles per unit volume of air). The near-surface OPS and OPC particle-volume PSDs ($\frac{dv}{d\log r} = \frac{4}{3} \pi r^3 \frac{dn}{d\log r} = \frac{4}{3} \pi r^3 \frac{dn}{d\log D}$) are analogous to the columnar particle-

⁸ To be clear about the definition of lidar ratio, we note that its general definition is $1/[\omega_0 p(\pi)]$ (with a Rayleigh / molecular value of $8\pi/3$) and that ω_0 and $p(\pi)$ are respectively, the single scattering albedo and scattering phase function at a scattering angle of π radians and where the integration of $p(\chi)/[4\pi]$ over 4π steradians is unity.

⁹ or more precisely, the radii of spherical particles that would be optically equivalent to irregularly shaped particles

215 volume PSDs ($dV/dlnr$) products of the AERONET inversion (columnar particle-volume per unit area) while the $v_c(0)$ parameter is analogous to the AERONET CM-integrated particle-volume density (“VolC-C” or V_c) product. Since we only consider events that are likely to be dust events (as evidenced by the lidar-measured presence of a dust plume) we will generally label $v_c(0)$ as $v_{dust}(0)$.

3.4 Correlation analysis

220 Indicators of the optical significance and remote sensing detectability of a dust event can, we would argue, be represented respectively by how dust-related τ_c^ℓ correlates with the KLRs OPS measurements of $v_{dust}(0)$ and how well τ_c correlates with dust-related τ_c^ℓ . Our dust (and cloud) classification methodology defined below is largely based on the coefficient of correlation between $v_{dust}(0)$, τ_c^ℓ and τ_c .

Results such as those of Hesaraki et al. (2017) empirically indicate that geometric statistics of AODs (histograms and 225 statistics computed in log-AOD space) are more representative than the arithmetic statistics of linear-AOD space and that a consequence of this is that R values should be larger (results that will, however, always be subject to the vagaries of low-sample or “low-N” statistics). In order to better understand the degree of coherency between the three different types of data, we analyzed their correlations in linear-AOD and log-AOD space as a function of different time-bin amplitudes (results are presented below).

230 3.5 Event classification

The classification methodology must clearly separate the optical effects of dust and clouds: the first step in this process is to isolate apparent dust plumes in the vertical profiles of the lidar. The dynamic process for arriving at a variable dust layer height (DLH) from the $\beta_{c,\sim}$ profiles is outlined in the Supplementary material (S2). An estimate of lidar-derived dust optical depth (τ_{dust}^ℓ) can then be computed by vertical integrations of the $\beta_{c,\sim}$ profiles from the surface to the DLH. We then argue 235 that τ_{cloud}^ℓ values (or at least the CM optical depth of anything but local dust) are obtained by vertically integrating the $\beta_{c,\sim}$ profiles from the DLH to LCH.

We focused on two levels of correlation: the use of $R_{log}(\tau_{dust}^\ell \text{ vs } v_{dust}(0))$ values as a means of identifying and characterizing optically significant dust events and $R_{log}(\tau_c \text{ vs } \tau_{dust}^\ell)$ values to identify those events that could be remotely 240 sensed by a passive ground- or satellite-based instrument¹⁰. In the latter case the high frequency τ_{dust}^ℓ values must be resampled to match the 1 minute time bins (3 minute intersample times) of the low frequency τ_c values: this process is described in Appendix A3. Our justification for the use of such a dust event flagging protocol is that correlation is a necessary (if insufficient) indicator of the presence of a dust event and that it is largely impervious to systematic instrumental issues

¹⁰ The latter correlation is complicated by AERONET cloud screening protocols: potentially strong dust-induced correlations might, for example be inadvertently eliminated by the Level 1.0 triplet processing or the Level 1.5 cloud screening process.

(calibration issues for example). Verification of correlation-based dust event flagging is usually supported (contextualized) by other types of indicators (the recording of strong basin winds, for example). We attributed the following event-classification codes for different, event-level periods of interest (POIs).

3.5.1 Optically significant (*D* class) dust

Our fundamental classification is that of a dust (*D*) class that appears to be optically significant at the columnar optical depth scale. A POI was defined as belonging to the *D* class if:

$$R_{log}(\tau_{dust}^{\ell} \text{ vs } v_{dust}(0)) \geq 0.5$$

This class basically requires that local KLRs OPS variations at the surface be at the same scale of variation as the columnar lidar optical depths (i.e. something that would not likely be true for dust turbulence scales ~ a few meters).

3.5.2 Optically insignificant (*U* class) dust

We labelled a POI that failed to satisfy the *D* class criterion as a *U* (unknown) event (this includes cases for which there were less than 10 matched OPS-lidar matched samples):

$$R_{log}(\tau_{dust}^{\ell} \text{ vs } v_{dust}(0)) < 0.5$$

3.5.3 *D* and *U* subclasses

The *D* classification rule leads to two subclass children: class *D* events that can and cannot be remotely sensed (respectively D_{RS} and D_{NRS}). In the former case we would argue that the potential for achieving the satellite-based remote sensing of a dust event must require that a passive ground-based measurement of a candidate dust plume (τ_c) must be significantly correlated with its lidar analogue. The D_{RS} subclass was accordingly defined as:

$$R_{log}(\tau_c \text{ vs } \tau_D^{\ell}) \geq 0.5$$

This means that the correlation must be roughly impervious to spatio-temporal sampling differences between the lidar and the photometric measure (including the fact that the photometric measure represents a completely different line of sight relative to zenith looking lidar). The complementary D_{NRS} subclass follows as:

$$R_{log}(\tau_c \text{ vs } \tau_D^{\ell}) < 0.5$$

It includes, by default, cases for which there were less than $N(\tau_c) = 10$ retrievals or for which the lidar indicates the presence of cloud ($\tau_{cloud}^{\ell} \geq 0.001$)¹¹. The *D* subclasses have their *U* subclass analogues: class *U* events that can and cannot be remotely sensed (respectively U_{RS} and U_{NRS}):

$$R_{log}(\tau_c \text{ vs } \tau_U^{\ell}) \geq 0.5$$

¹¹ the 0.001 minimum is an order of magnitude estimate of τ_c sensitivity to real physical CM changes (an estimate based on experiential evidence such as the seasonal variations observed by AboEl-Fetouh et al., 2020)

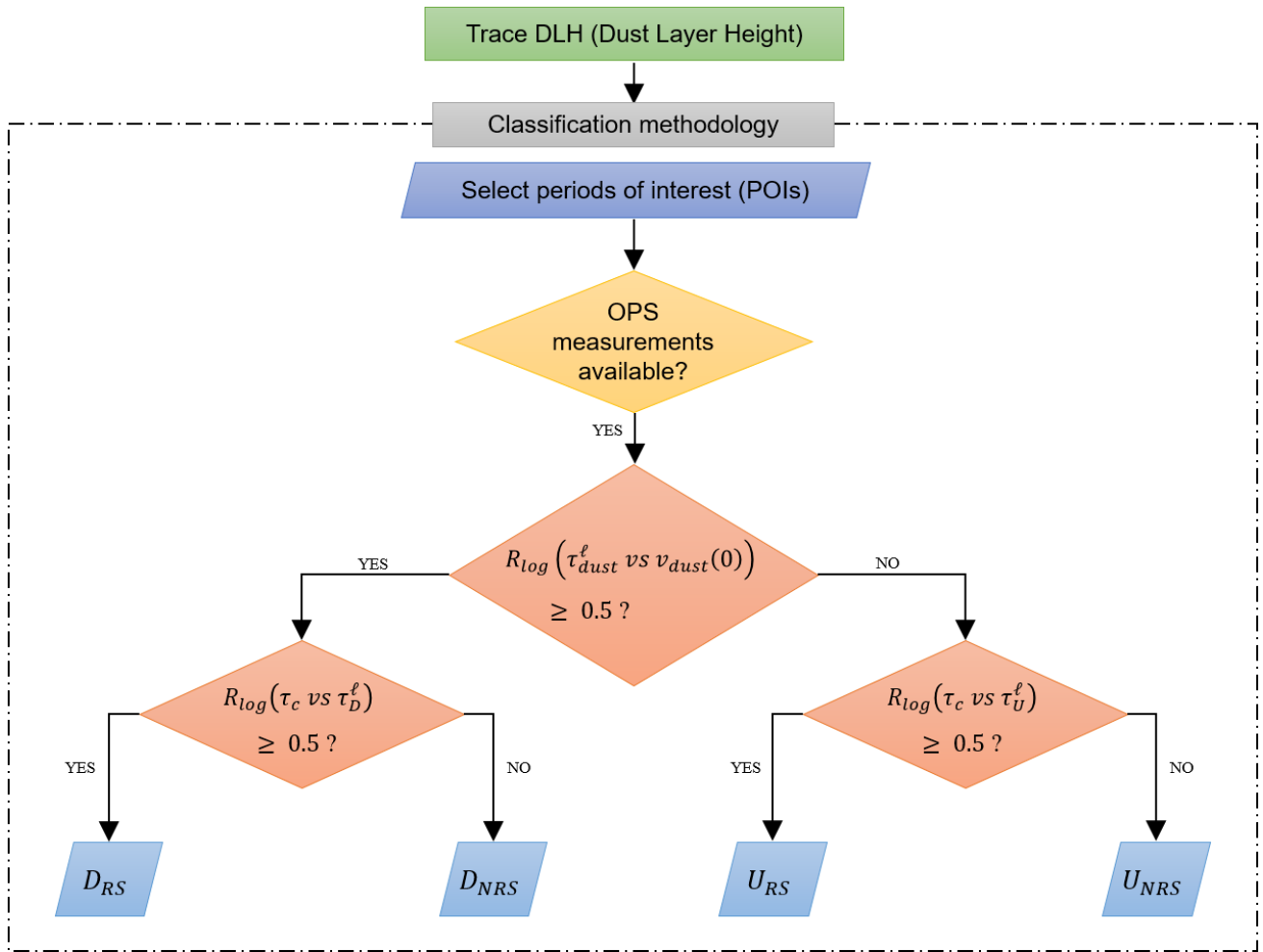
270 $R_{log}(\tau_c \text{ vs } \tau_U^{\ell}) < 0.5$

The U_{RS} subclass represents cases where the correlation between τ_c and τ_{dust}^{ℓ} indicates the presence of a detectable remote sensing event of an unknown nature (“unknown” at least in the context of a “ D ” classification that is tied to threshold values of $R_{log}(\tau_{dust}^{\ell} \text{ vs } v_{dust}(0))$). The U_{NRS} subclass represents a non-event that defies both a dust and a remote sensing label.

275 Figure 2 summarizes the dust classification paradigm in a more heuristic flowchart manner. For the sake of simplicity, the special D_{FPC} and D_{GEN} subclasses defined immediately below have been omitted from the flow-chart.

3.5.3 Special classes

A special false positive cloud subclass (D_{FPC}) was defined for which the AERONET cloud screening process appeared to eliminate real optical depth variations induced by a dust event: class D events for which $N(\tau_c) \leq 10$ and for which τ_{cloud}^{ℓ} indicates no cloud. A special “generic” dust subclass (D_{GEN}) was defined to include events that were identified, with a
280 reasonable certainty using circumstantial evidence. The circumstantial evidence could include combinations of, for example, lidar profiles, reports from measuring teams on the ground, RGB satellite images that visually show dust plumes over Lhù’àn Mân’ (the PlanetScope image of Fig. 1 for example), information from auxiliary measurements such as downslope wind velocity or PM10 devices, etc.



285 Figure 2: Flow-chart of the classification methodology described in the text. The different class symbols are defined directly above the flow chart. The $N(\tau_c)$ threshold is 10 samples. The D_{FPC} and D_{GEN} subclasses would be supplementary branches (not shown) from the “No” of the upper-level $R_{log}(\tau_{dust}^l vs v_{dust}(0)) \geq 0.5$ decision diamond.

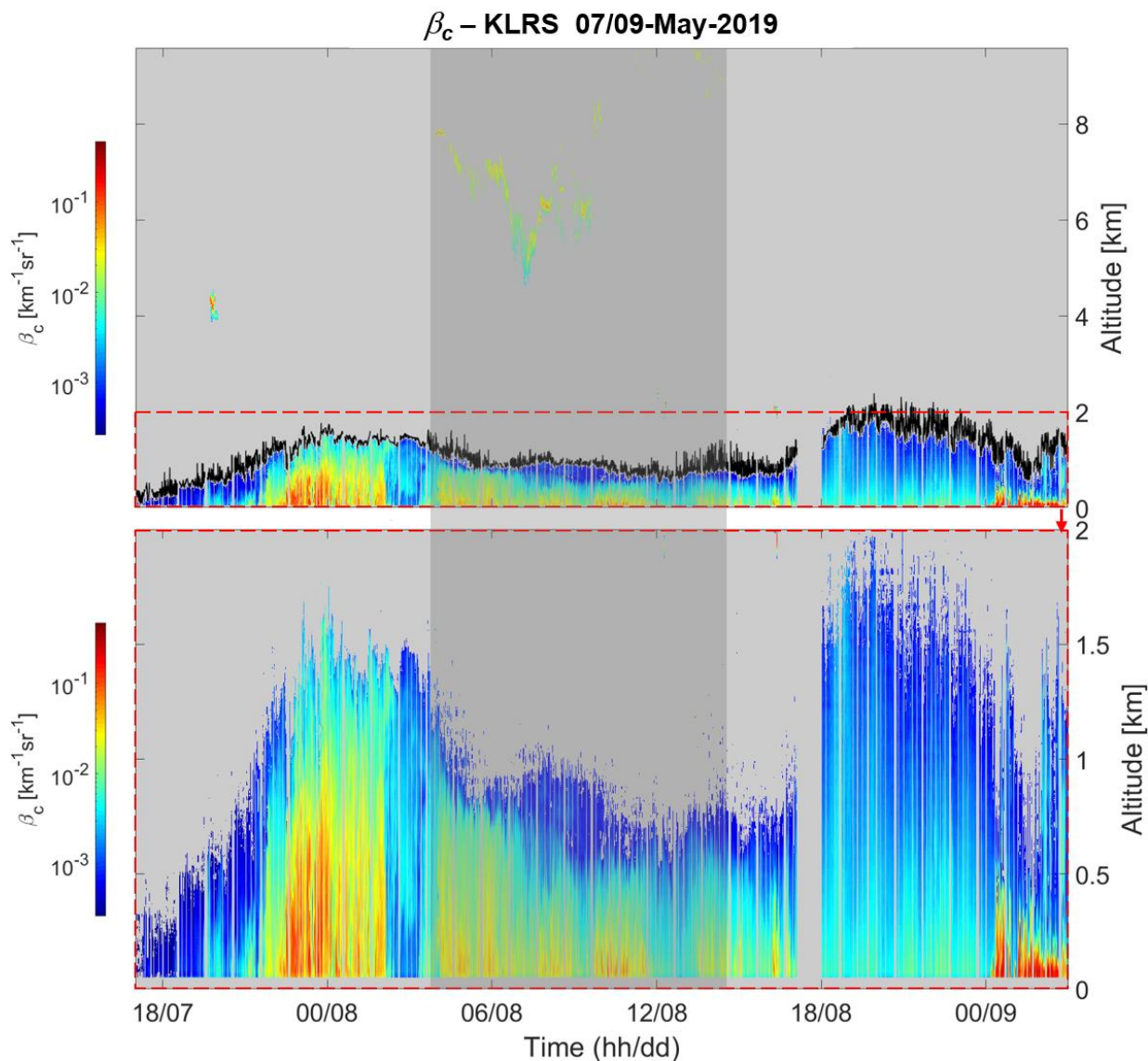
4 Results

4.1 Lidar measurement overview

290 Figure 3 shows a $\beta_c(z)$ profile¹² over a time period in May of 2019 that includes a number of interesting events. Our intent here is (i) to illustrate the profile attributes (notably the logarithmic color legend) during a diversity of events as well as the fact that dust plume heights were generally less than 2 km (red-dashed line) and (ii) to give the reader an event-continuity

¹² Actually the profile is that of the $\beta_{c,\sim}(z)$ parameter of Eq. (2): we dropped the “ \sim ” subscript in our profile figures for the sake of simplicity.

295 perspective that is not always evident in the shorter term (POI-driven) daily profiles found in the Supplementary material (S6). One can observe a relatively strong-backscatter plume with a maximum height at $\sim 00/08$ whose height decreases in altitude and optical impact during the typical nighttime¹³ shrinking of the boundary layer and then increases to a peak at $\sim 20/08$ UTC (followed by an apparently strong but very low-altitude plume beginning around 00/09). Cloud formation can be observed between about 5 and 9 km altitude during the nighttime.



¹³ The “white-night” period that we defined as the sun being below 10° elevation (indicated by the darker grey shading)

300 Figure 3: $\beta_c(z)$ profile, from 0.05 to 9.6 km (top panel) and a zoom from 0.05 to 2 km (bottom panel) during a selected time period in May 2019 (the red-dashed rectangles underscore the 0.05 to 2 km range in both panels). The times are UTC (local “Pacific daylight” time is 7 hours behind the UTC time). The grey background corresponds to lidar profile pixels that are set to NaN (not a number): these are the result of signal-to-noise ratio (SNR) threshold flags employed to eliminate excessively noisy data (Newsom & Krishnamurthy, 2020). The black color that is evident at the top of the plume in the upper panel shows the automated estimate of dust layer height (DLH). The region of darker grey shading corresponds to the nighttime (see the text for details)

305 4.2 Classification of dust events

4.2.1 Results of the correlation analysis

In order to investigate the influences on $R_{log}(\tau_{dust}^\ell vs v_{dust}(0))$ variability (and thus better understand its impact on the classification methodology) we computed (as discussed in Sect. 3.4) both linear and log space (arithmetic and geometric) correlations as well as the dependence of those correlations on time bin resolution. Sample arithmetic and geometric correlation coefficient values as a function of temporal bin resolution are shown in Supplementary material (S3). Geometric correlation coefficients (R_{log}) were typically of the same order as or better than arithmetic coefficients (R) in the presence of more than one decade of $\tau_{dust}^\ell vs v_{dust}(0)$ variation : we accordingly used this as support for reporting correlation coefficients in geometric statistics space. This choice was supported by analyses showing that ground- and satellite-based AOD histograms were better described by geometric means and standard deviations (O’Neill et al., 2000 and Sayer & Knobelspiesse, 2019 and references cited therein).

315 Aside from the obvious limitations of low-N (low sample number) statistics, no strong dependence on time-bin resolution was found. We accordingly chose to employ the highest bin-resolution¹⁴ as the basis for our classification analysis (the selection of the high bin-resolution case being also justified on the general principle of wishing to minimize the elimination of high frequency lidar data that might have physical significance). We believe that this R_{log} -dependent classification approach is as independent as it can be from issues such as instrument calibration or changes in the optical or microphysical strength of the dust plume: the verification of this affirmation in terms of other sites or other seasons is a step that we are actively pursuing.

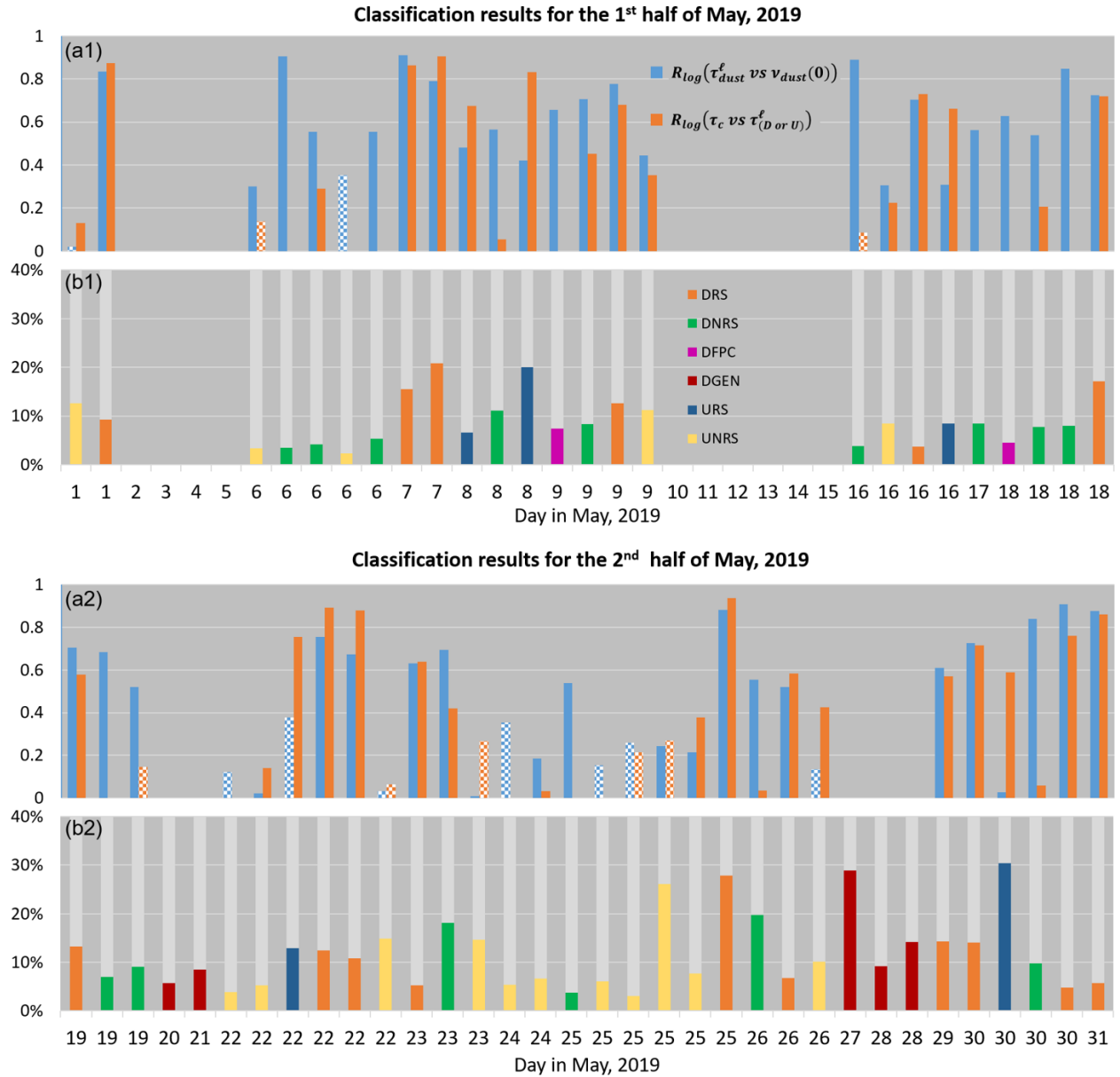
4.2.2 Subclass statistics

325 The POI subclass results for the complete month of May 2019 are shown in Fig. 4 (b1 and b2) while the corresponding correlation coefficient values are shown in Fig. 4 (a1 and a2). As one might expect for a true dust event, the results often show a degree of correlation between the blue and orange bars¹⁵. Other examples of note are the two D_{NRS} events of negative $R_{log}(\tau_c vs \tau_D^\ell)$ (see Sect. 4.2.3 for optical details on one of those events). Details of a May 8 U_{RS} event are discussed in Sect.

¹⁴ where the lidar OPS measurements are resampled to CIMEL averaging bins of 1 minute and inter sample gaps of 3 minutes

¹⁵ between the class-determining correlation coefficients of $R_{log}(\tau_{dust}^\ell vs v_{dust}(0))$ and $R_{log}(\tau_c vs \tau_{(D or U)}^\ell)$

4.2.4. We also note the existence of five D_{GEN} events (identified using the lidar profiles of the Supplementary material (S6) as well as the PlanetScope image on May 27).



330

Figure 4: May 2019 results: $R_{log}(\tau_{dust}^{\ell} vs v_{dust}(0))$ and $R_{log}(\tau_c vs \tau_{(D or U)}^{\ell})$ for the a1 and a2 (upper) profiles. D_{RS} , D_{NRS} , D_{FPC} , D_{GEN} , U_{RS} , and U_{NRS} subclasses for the b1 and b2 (lower) profiles (the products of the classification scheme presented in Fig. 2). The subclasses are represented as duty cycles (event duration as a percent of 24 h). The hatched bars of the a1 and a2 profiles represent negative R values.

335 The light grey bars highlight the link between the subclasses and the R_{log} values that served to define those subclasses. See Sect. 3.5 for details on the R_{log} correlation coefficients as well as the D and U subclasses.

4.2.3 Cloud and pseudo-cloud illustrations during class D events

In many cases the CIMEL processing resulted in no or very few AODs during periods when clouds were identified in the lidar profile (this, in spite of there being no nominal cloud screening for the Level 1.0 SDA⁺ product). However, there is a “triplet” filter at the beginning of the data processing chain which eliminates highly variable triplet ODs during the CIMEL 1
340 minute bin-averaging period (see Giles et al., 2019). These highly variable ODs are not only restricted to clouds: they also included extremely variable CM dust AODs during periods of the day that were largely cloud-free (what would amount to strong spatially variant dust plumes crossing the FOV of the CIMEL)¹⁶. This problem was also reported by Evan et al. (2021).

Figure 5 illustrates two types of D subclasses (between the black- and red-dashed vertical lines). The lidar captures cloud and dust intrusions between the black vertical lines (cloud layer ~ 2 km and dust layers below 2 km) during which there are
345 no SDA⁺ retrievals. This is an example of largely legitimate cloud screening by triplet filtering of AODs prior to promotion to Level 1.0 AODs (the significant high frequency variation of the green τ_{cloud}^{ℓ} curve supports this affirmation). The triplet filtering between the red vertical lines (encompassing a large cloud-free event) retains, on the other hand, a significant number of dust-correlated τ_c values to yield a D_{RS} event. Note, however, that the Level 1.5 product (not shown) eliminates nearly all retrievals associated with the Level 1.0 D_{RS} event: this amounts to an example of a D_{FPC} event for Level 1.5 AODs (Fig. 4 of
350 Evan et al. (2021) illustrates what is likely a D_{FPC} event resulting from aggressive cloud screening being applied to Level 1.0 AODs). This discrepancy between the Level 1.0 and Level 1.5 subclasses indicates an excessive sensitivity of Level 1.5 cloud screenings to optical variations that are most likely local dust variations. This is, in fact, a situation where it is better to minimize cloud-screening protocols if the ultimate goal is detection and characterization of highly variable local dust.

Another cloud impact example is associated with the two negative $R_{log}(\tau_c \text{ vs } \tau_D^{\ell})$ cases referred to above: it is instructive
355 to understand the optical dynamics of one of these cases (both of which were plagued by the presence of multi-altitude cloud). The POI 16-1 event at the beginning of May 16 (cf. the upper profile on page 8 of the Supplementary material, S6) showed strong τ_{cloud}^{ℓ} variation associated with¹⁷ vertically thin but optically thick clouds at $< \sim 2$ km altitude whose triplet impact appeared to create large gaps in the temporal variation of τ_c . In contrast, more homogeneous clouds at ~ 4 km (whose τ_{cloud}^{ℓ} values appear between gaps of the 2 km clouds but which themselves were interspersed with gaps induced by the strong
360 attenuation of the 2 km clouds) sometimes evaded the triplet filtering. The coupling of these two different types of cloud interference did much to eliminate any possible covariation between the remaining τ_c points and τ_D^{ℓ} .

¹⁶ At the other cloud screening extreme are false negative clouds associated with homogeneous clouds such as cirrus that go undetected. V3 processing incorporated some significant changes in an attempt to deal with this problem (Giles et al., 2019).

¹⁷ ~ 100 m in vertical thickness and optical depths $> \sim 1$. The β_{cloud} values associated with those clouds are removed in the lower profile of slide 8 (as part of the DLH process).

β_c - KLRS 18/19-May-2019

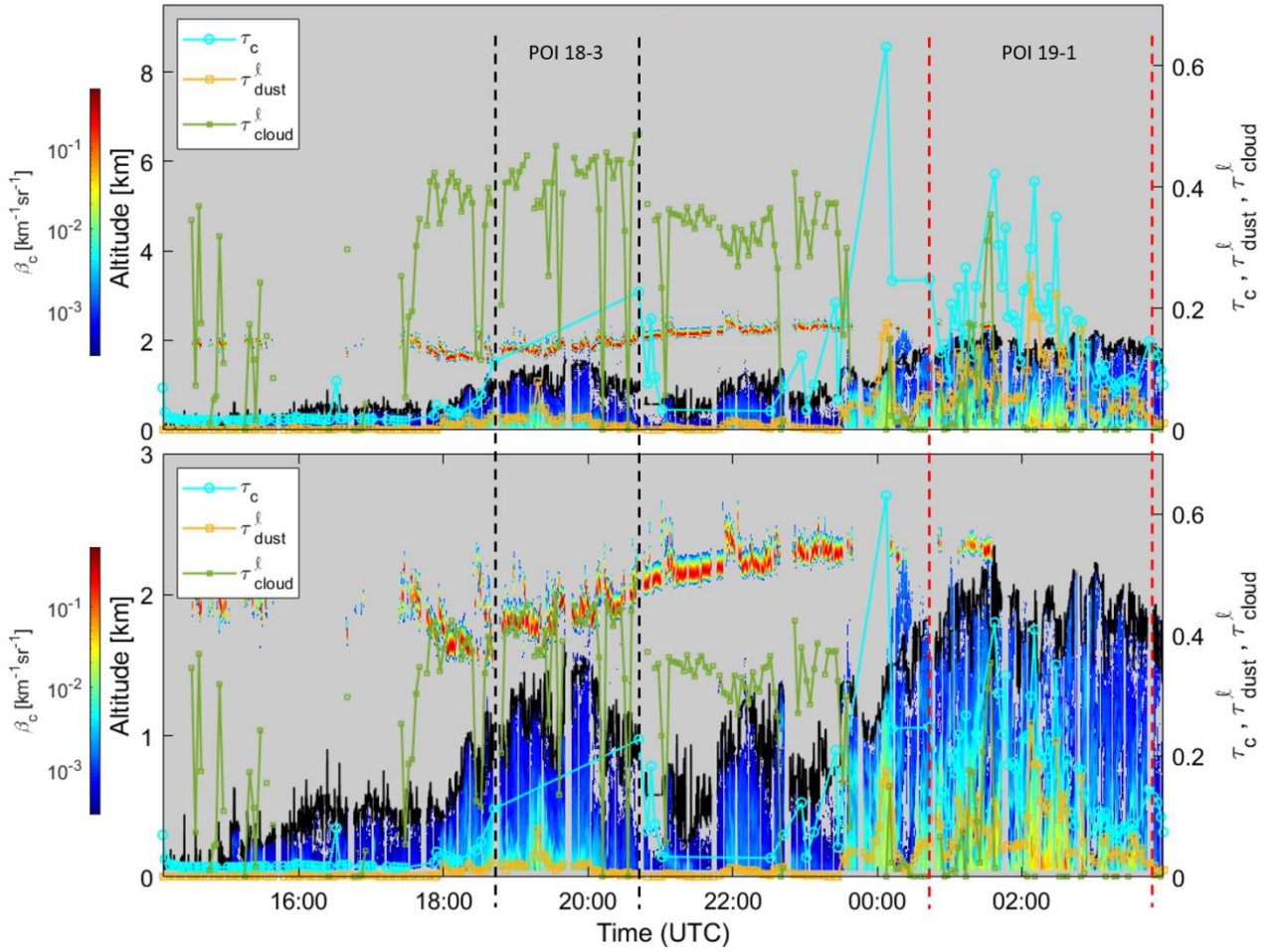


Figure 5: *D* subclass events of May 18, and the beginning of May 19, 2019. The top profile above shows the entire lidar altitude range while the bottom profile is restricted to the 0–3 km range in order to better appreciate the details of the dust plume (below ~ 2 km) and the thin cloud layer hovering around 2 km. The black and red-dashed vertical lines encompass two *D* subclass events (POI 18-3 and POI 19-1). The former event shows that no τ_c value survived the triplet filtering while the latter D_{RS} case indicates substantial τ_c vs τ_D^l correlation ($R_{log}(\tau_c \text{ vs } \tau_D^l) = 0.58$).

365

4.2.4 Remote sensing threshold for the detection of local dust

Figure 6 shows a plot of τ_{dust}^l vs $v_{dust}(0)$ for all class *D* and *U* events during May of 2019. The graph suggests, for a certain fraction of the events, an apparent τ_{dust}^l insensitivity (“bottoming out”) to $v_{dust}(0)$ variations below an apparent $v_{dust}(0)$ threshold of $\sim 10^{-11} \mu\text{m}^3 \mu\text{m}^{-3}$. However the subclass scattergrams of the Supplementary material (S4) suggest a more nuanced threshold: the U_{RS} and U_{NRS} scattergrams, in particular, show “bottoming out” $v_{dust}(0)$ thresholds that can be anywhere in the 10^{-11} – $10^{-10} \mu\text{m}^3 \mu\text{m}^{-3}$ range with a respective τ_U^l range of 0.001–0.1. AboEl-Fetouh et al. (2020) showed pan-

370

Arctic τ_c values (regional-scale, multi-year geometric means) whose τ_c variation¹⁸ was as small as ~ 0.001 . That the
375 τ_U^ℓ bottoming out values of the U_{RS} and U_{NRS} scattergrams are generally well above this value suggests that the apparent lack
of τ_U^ℓ variability is attributable to very local, near-surface dust dynamics that are at the margins of column-scale detectability.
This suggestion is consistent with the observation of Huck et al. (2023) on the importance of local scale variability during
Lhù'àn Mân' dust storms.

The POI 8-3 event of Fig. S1 underscores the relevance of the U_{RS} subclass assignment (of $R_{log}(\tau_c \text{ vs } \tau_U^\ell)$ being large):
380 the apparent τ_U^ℓ bottoming out of all the point clusters in the U_{RS} scattergram of Fig. S4 is more about an apparently narrow
spread driven by the densely packed τ_U^ℓ log scale. The appearance of the POI 8-3 lidar profile and the temporal covariation of
 τ_c and τ_U^ℓ (associated with the orange points of Fig. S4) is strongly suggestive of an optically weak dust plume for which the
covariation of τ_c and τ_U^ℓ is not some statistical artefact. This does not detract from the argument of local scale
 $v_{dust}(0)$ variability being uncoupled from the columnar variability: it simply says that the physical significance of the
385 columnar variability can occur within the (apparently narrow) τ_U^ℓ spread of the point clusters in the U_{RS} scattergram.

¹⁸ Variations that appeared to be robustly sensitive to certain natural Asian dust events

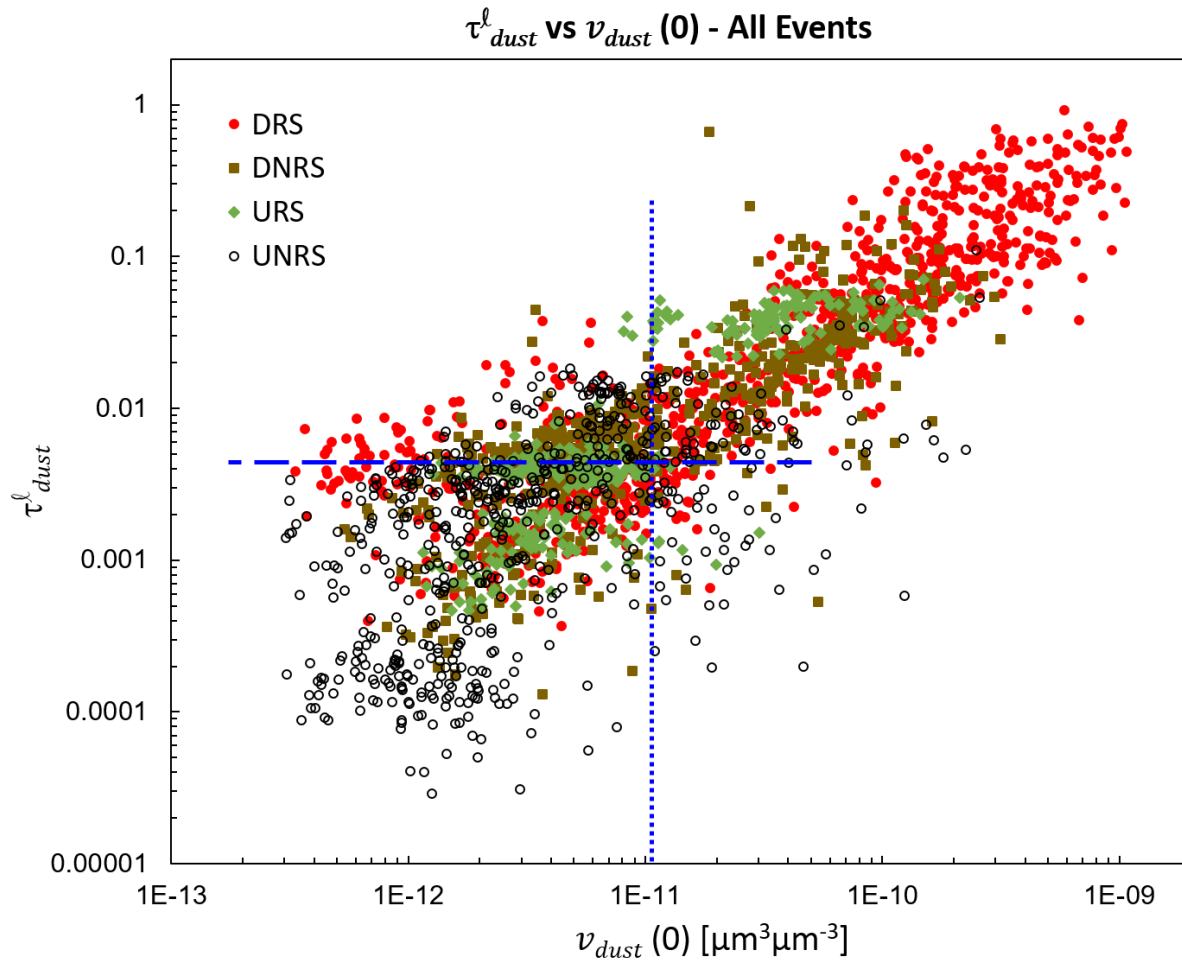


Figure 6: Plot of τ_{dust}^l vs $v_{dust}(0)$ for all class *D* and *U* events during May of 2019. Note that this ensemble of data excludes points belonging to the special D_{FPC} and D_{GEN} subclasses. The blue dashed horizontal line represents the apparent τ_{dust}^l “bottoming out” effect while the vertical dotted line represents the $v_{dust}(0)$ threshold (see text for details)

390 4.3 Parameterization of dust plume properties

4.3.1 Lidar ratio

4.3.1.1 Prescribed lidar ratio

The CM r_{eff} values for the whole month of May 2019 were calculated for all individual KLRS OPS PSDs that were part of class *D* POI events. A temporal plot of those individual $r_{eff,c}$ ($r_{eff,D}$) values can be seen in Fig. 7. The averaged class *D* results for the month of May were (as per the Fig. 7 legend) found to be: $\langle r_{eff,D} \rangle \pm \sigma_D(r_{eff,D}) = 2.26 \pm 0.23 \mu\text{m}$.

395

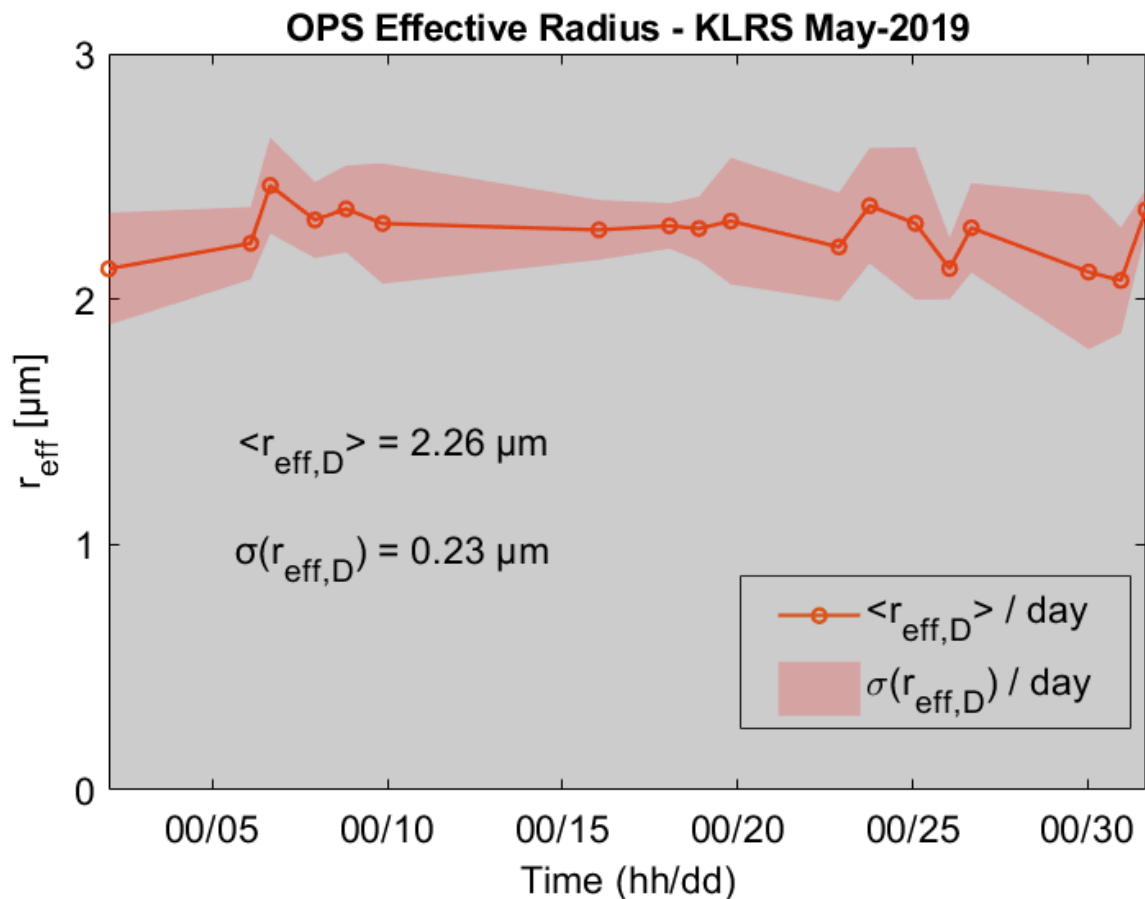
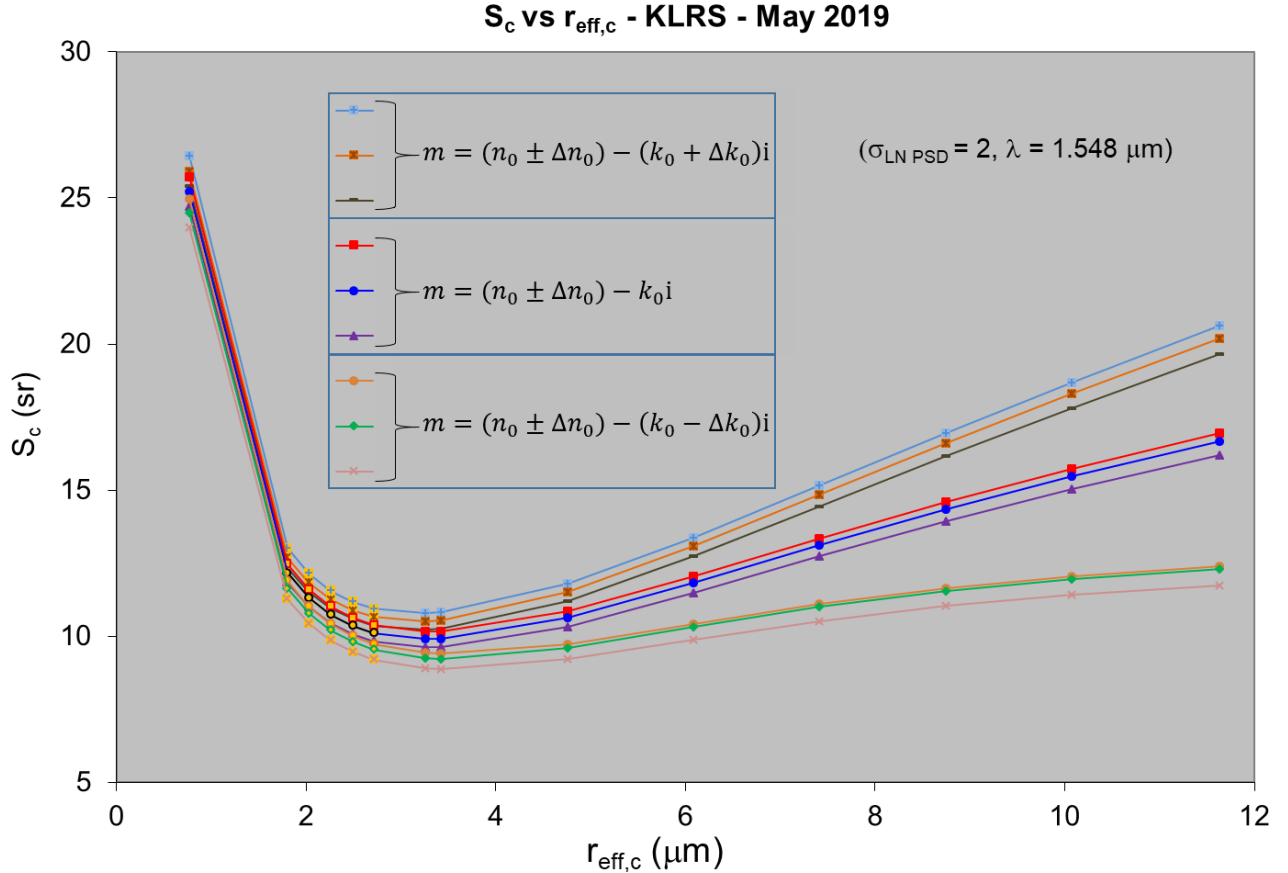


Figure 7: Variation of OPS-derived, class- D , r_{eff} values during the month of May 2019.

Clay, feldspar, and then quartz minerals are the major constituents of the PM₁₀ dust particles from the emissions in the Kluane Lake region (Bachelder et al., 2020; King, 2023). To derive the mean refractive index and the uncertainty for those values, we followed the method of Baldo et al. (2020) using the volumetric-average refractive index based on the relative volume fraction weighted refractive indices of the minerals found within the dust sampled at the site, through X-ray diffraction, assuming an internally mixed sample (Formenti et al., 2014). The result, which we took to be representative of the Lhù'ààn Mân' region, was a mean refractive index of $m = 1.5371(\pm 0.0028) - 0.00075(\pm 0.00072) i$ at the 1.548 μm lidar wavelength.

Figure 8 shows the range of lidar ratio curves given the mean and uncertainties of the down valley estimates of refractive index and a 0–12 μm range of $r_{eff,D}$ values (the OPS-derived $r_{eff,D}$ values and their uncertainties appear as orange circles). All lidar ratios were computed using a (spherical particle) Mie code (Evans, 1994) integrated over a lognormal PSD (see Sokolik & Toon, 1999 for a typical formulation and values of that analytical PSD). We employed Sokolik & Toon's geometric

standard deviation for dust (" σ_j " = 2) and forced the lognormal geometric mean (" r_{0j} ") to yield a computed lognormal-PSD effective radius that matched the OPS-derived $\langle r_{eff,D} \rangle$ values. The colored curves of Fig. 8 nicely demonstrate the impact of the real and imaginary parts of the refractive index on the lidar ratio computations (a somewhat balanced impact at small $r_{eff,D}$ in the neighbourhood of the OPS derived values of $r_{eff,D}$ with a much stronger impact of the complex part of the refractive index at larger radii). This yielded a prescribed lidar ratio estimate of $S_D^p = 10.7 \pm 0.9$ sr (where the uncertainties were derived by combining the $r_{eff,D}$ and refractive index uncertainties).



415 Figure 8: Mie (spherical-particle) computations of lidar ratio based on the refractive index (n) value from above. The orange circles represent $r_{eff,D}$ changes from $\langle r_{eff,D} \rangle - 2\sigma(r_{eff,D})$ to $\langle r_{eff,D} \rangle + 2\sigma(r_{eff,D})$ in increments of $\sigma(r_{eff,D})$. The refractive index parameters of the figure are $n_0 = 1.5371, \Delta n_0 = 0.0028, k_0 = 0.00075,$ and $\Delta k_0 = 0.00072$. $\sigma_{LN PSD}$ refers the standard deviation of the lognormal PSD that was employed in the Mie computations.

420 4.3.1.2 Evaluation / validation of the prescribed lidar ratio

Individual $S_{D_{RS}}$ values for each D_{RS} event were computed as per Appendix A1 (i.e., weighted best estimates of separate $S_{D_{RS}}$ computations for each event where weights are defined by the inverse square of $S_{D_{RS}}$ regression residuals). The overall weighted result for the entire month of May 2019 was $\langle S_{D_{RS}} \rangle_\omega \pm \sigma_w(S_{D_{RS}}) = 28.0 \pm 3.3$ sr. The weighted mean, $\langle S_{D_{RS}} \rangle_\omega$, is

roughly three times the S_D^p value of 10.7 ± 0.9 sr reported above (i.e. shows a positive bias). While the overall apparent effect
 425 of the weighting scheme, as seen in Fig. S5, was to reduce the variation as a function of increasing weight it did not objectively
 achieve satisfactory agreement with S_D^p . A measure of closer agreement with the S_D^p value (a lesser positive bias) was obtained
 by setting a higher standard on theregressions or the amplitude of the slant path lidar optical depth¹⁹: these two constraints
 yielded $\langle S_{D_{RS}} \rangle_\omega$ values of 19.1 ± 2.3 sr and 20.3 ± 2.6 sr for $R_{log} > 0.9$ or slant path optical depth > 0.05 respectively.
 We note that the comment by Huck et al. (2023) concerning the frequent missing of plumes by the CIMEL (or presumably
 430 only capturing a portion of the plume in the CIMEL FOV) is actually a counter dynamic to the positive bias: a problem of
 partially missing the plume would actually help to reduce the bias.

Given the persistence of this positive bias we sought to determine whether S_D^p could, in fact, be underestimated. A
 significant increase in its computed value can be obtained by assuming the general presence of larger, optically-significant
 dust particles in the plumes. Figure 8 indicates that an $r_{eff,D}$ value $\sim 11\text{--}12$ μm and the higher value of the imaginary index of
 435 refraction determined from the dust speciation result would push the S_D^p to values ~ 20 sr (a value commensurate with the
 “higher standard” argument in the previous paragraph). The OPS instrument with its upper limit of 5 μm radius (see Sect.
 4.3.2.1 below) is incapable of measuring such a PSD contribution while the few AERONET inversions that were available
 showed a dust mode of increasing radius (up to 7 μm) with increasing (but weak) values of dust optical depth (see the following
 section). Ranjbar et al. (2021) reported on the presence of dust particles $>\sim 15$ μm radius²⁰ for CloudSat / CALIOP (DARDAR)
 440 retrievals over Lake Hazen dust plumes in the Canadian high Arctic (a drainage-basin environment analogous to that of
 Lhù'àn Mân'). At southern latitudes, optically-significant lidar profiles whose volume-median radius was $>\sim 8$ μm have been
 observed for near-source Saharan dust plumes (the Fig. 13, May 20–28 results of Weinzierl et al., 2009 and, as evidence of
 optical significance, the corresponding column averaged lidar ratios of Esselborn et al., 2009).

4.3.2 AERONET inversions

445 Table 1 lists key AERONET CM inversion products acquired during D class events for the month of May 2019 (optically
 based inversion products that were spectrally extrapolated to the 1.548 μm lidar wavelength from values at the shorter inversion
 wavelengths). The relatively few retrievals underscore the sometimes-frustrating disparity of dealing with the information rich
 AERONET-inversion product when it is associated with few inversions during an event of interest (coupled with the fact that
 the CM AOD were generally weak: $\tau_{c,inv} < 0.15$). This speaks to the difficulty in extracting significant numbers of AERONET
 450 retrievals even on the Table 1 days with the largest $\tau_{c,inv}$ values. However, if the information we want is of an intensive-

¹⁹ $\langle m \rangle \langle \tau_c^\ell \rangle$ where $\langle m \rangle$ is the POI-averaged airmass of the sun: the hypothetical case where the lidar is probing a plane parallel
 plume at the same zenith angle as the sun.

²⁰ the lower limit of 15 μm being determined by CloudSat radar detection limitations

parameter nature (effective radius, PSD radius attributes like PSD-peak positions, etc.) then we can aspire to extract representative values that vary little across a month (that don't need to be monitored at a high sampling rate).

455 Table 1: AERONET May 2019 CM inversion products for all retrievals classified as D_{RS} events (ordered according to decreasing $\tau_{c,inv}$). With respect to the single U_{RS} (POI 8-3) case: the rather dominant $\tau_{c,inv}$ value and the appearance of its lidar profile in the Supplementary material (S6) suggest that it is most likely a dust event (it could, for example, be attributed a D_{GEN} subclassification). The $\tau_{c,inv}$ values were derived from a spectral extrapolation (using log-log regressions) from the four AERONET inversion wavelengths to the 1.548 μm lidar wavelength. The colors associated with the different dates represent retrievals for the 6 largest $\tau_{c,inv}$ values (the same colors are used to identify the associated PSDs of Fig. 9).

Date (2019)	Time (UTC)	POI	$\tau_{c,inv}$	Sub- class	$V_{c,inv}$ ($\mu\text{m}^3 \mu\text{m}^{-2}$)	$r_{eff,c,inv}$ (μm)	m_r	m_i
08-May	20:12:51	8-3	0.144	U_{RS}	0.778	3.262	1.600	0.001
02-May	00:48:49	1-2	0.048	D_{RS}	0.130	1.816	1.597	0.007
02-May	00:12:48	1-2	0.041	D_{RS}	0.096	1.639	1.600	0.005
07-May	19:12:50	7-1	0.028	D_{RS}	0.053	1.317	1.619	0.003
09-May	22:12:50	9-3	0.023	D_{RS}	0.069	1.880	1.600	0.004
07-May	18:12:51	7-1	0.020	D_{RS}	0.038	1.318	1.600	0.001
22-May	17:48:51	22-4	0.016	D_{RS}	0.050	1.854	1.525	0.008
22-May	19:12:52	22-4	0.016	D_{RS}	0.044	1.692	1.546	0.010
22-May	18:12:53	22-4	0.015	D_{RS}	0.045	1.741	1.504	0.008
25-May	22:12:50	25-6	0.015	D_{RS}	0.037	1.656	1.600	0.011

460 4.3.2.1 Intensive parameters from AERONET inversions

Figure 9 shows the set of PSDs corresponding to the retrievals of Table 1. One can observe bimodal CM peak positions near 1.3 and 5.0 / 6.6 μm (bin centers of respectively bins 13 and 18 / 19 of the AERONET inversion). In general, there appears to be a trade-off between the 1.3 and 5.0 / 6.6 μm peaks depending on the strength of the relative contributions to each peak. AboEl-Fetouh et al. (2020) ascribed the presence of a 1.3 μm component to the springtime incursion of Asian dust over six
465 AERONET stations spread across the North American and European Arctic (springtime being largely represented by April and May in their monthly averaged PSDs). The 6 largest $\tau_{c,inv}$ cases of Table 1 arguably represent the strongest local dust contributions. Four of these values are more dominated by the 5.0–6.6 μm peak while the other two are sufficiently weak to be dominated by a stronger 1.3 μm peak. The $r_{eff,c}$ values of Table 1 represent a compromise driven by the 1.3 and 5.0–6.6
470 μm peak positions (where the importance of the latter peak tends to increase with increasing $\tau_{c,inv}$). These $r_{eff,c}$ values (with an average of 1.87 μm) are somewhat less than the OPS-derived mean of 2.26 μm .

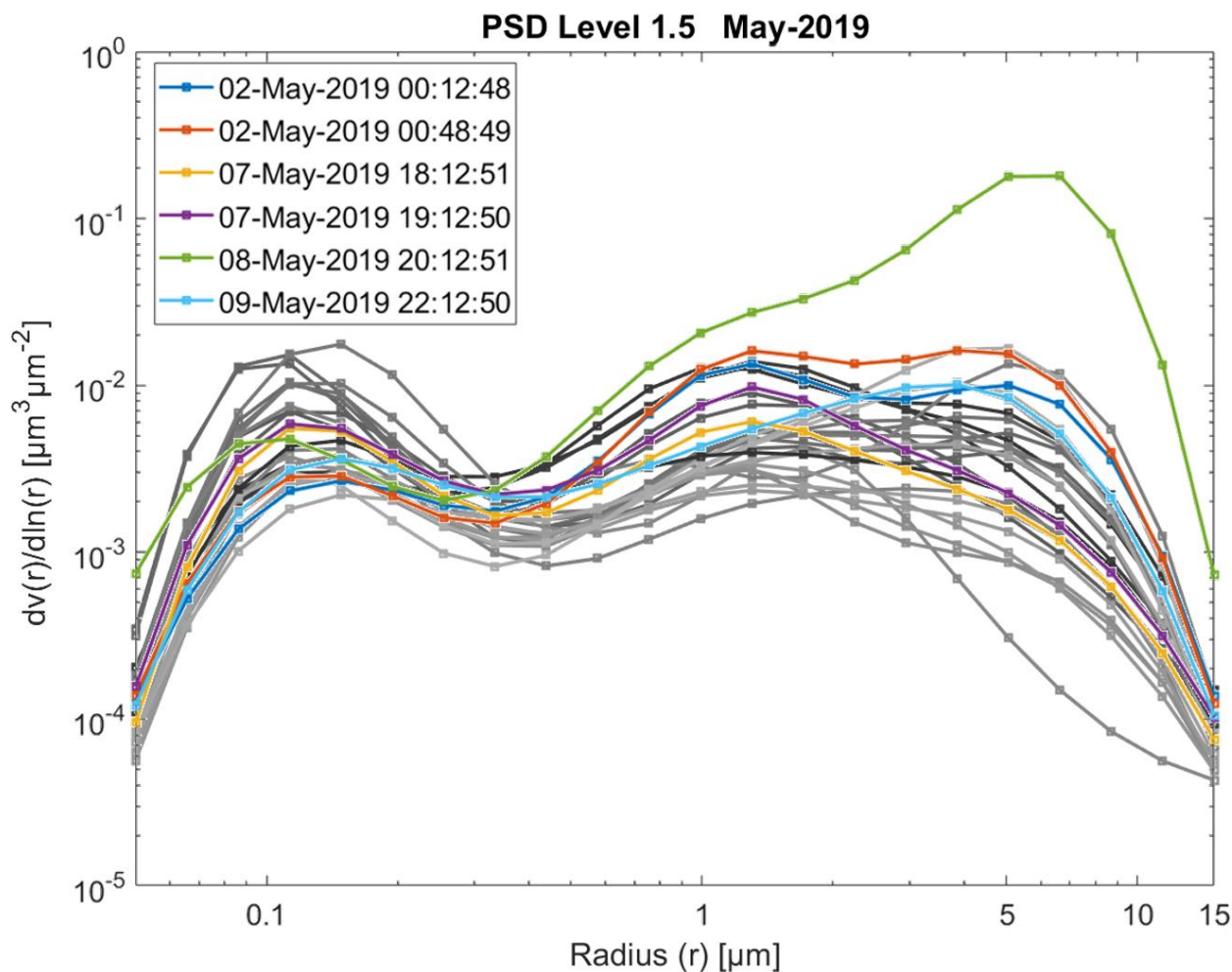
The suggestion that the AERONET 1.3 μm PSD peak is due to Asian dust needs to be contextualized by a relatively consistent, neighbouring peak at the 1.75 μm OPC bin (radius) center that was often recorded by the two DV units (see the

Supplementary material (S7) to observe the daily ensemble of OPS PSDs at KLRS and the OPC PSDs at the DV site on the six days corresponding to the 6 largest $\tau_{c,inv}$ events of Table 1). That peak was not observed by the OPS: the KLRS ensemble of PSDs on the six days in question could be best described as a broad modal feature whose form was quite stable but whose amplitude was highly variable. The broad nature of that modal feature inhibits any simple characterization (one cannot readily select a significantly robust modal peak that stands above the other PSD values in neighbouring bins). In fact, it appears to be common to the KLRS and DV sites if one views the 1.75 μm DV peak as a perturbation atop of that feature. Given the lack of even a 1.75 μm peak at the KLRS site and the ubiquitous nature of the 1.3 μm peak over the North American and European Arctic (AboEl-Fetouh et al., 2020) it is likely that the 1.3 μm AERONET peak is associated with springtime Asian dust. Finally, we would note that the broad CM feature might well be dynamically associated with the 5.0–6.6 μm AERONET inversion peak (with the OPS effective radius arguably being smaller than the AERONET inversion effective radius due to its 4.5 μm , bin-center, cutoff radius).

The significance of this result (in spite of our intensive parameter arguments at the beginning of this section) is necessarily brought into question by having only a handful of PSD retrievals over the whole month of May (and only one single retrieval with a dominant 6.6 μm component). In addition to this constraint on the number of retrieved PSDs, the $\tau_{c,inv}$ contribution of a 6.6 μm peak will generally be dominated by the $\tau_{c,inv}$ contribution of the 1.3 μm peak²¹. The few retrievals and their low $\tau_{c,inv}$ values are likely attributable to the cloud screening process of the AERONET inversions (whose constraints are commonly known to be more stringent than the cloud-screening protocol for AODs; this arguably amounts to the assignment of a D_{FPC} subclass in the case of the inversion processing stream).

The values of the real part of the refractive index in Table 1 are clearly susceptible to retrieval saturation issues (most notably the evident flatlining at a value of 1.6). The values of the imaginary part of the refractive index are highly variable. In general, one cannot ascribe much confidence to the May 2019 refractive index values: the AERONET U27 inversion-error product described by Sinyuk et al. (2020) shows no values (corresponding to a code of “-999”) for the real and imaginary parts of the refractive index (and the derived single scattering albedo). The authors indicate that no U27 values are reported “for any of the retrieved parameters” subject to a “boundary hit” (lower and upper limits of 1.33 to 1.6 represent such boundaries for the real part of the refractive index). Finally, we would note that, the comments made above concerning the behavior of the Fig. 9 PSDs are virtually unchanged if we restrict the retrieved PSDs to those that are not subject to “boundary hits” of the real part of the refractive index.

²¹ It is easy to approximately show, using Mie calculations and a refractive index ~ 1.6 (employing the approximate AERONET retrieval value for optical consistency) that the extinction efficiency associated with the AERONET particle-volume distribution (whose product, integrated over radius, would yield $\tau_{c,inv}$) is significantly larger at 1.3 μm radius (see for example, Hansen & Travis, 1974 for a definition of “efficiency factor”, the parameter analogous to what we call extinction efficiency).



500

Figure 9: AERONET-inversion PSDs ($dV/dlnr$) corresponding to the retrievals listed in Table 1 (the colored PSD curves correspond to the colors of Table 1). The grey-colored curves include the non-colored entries of Table 1 as well as all other May 2019 retrievals that were not assigned to the D_{RS} subclass.

4.3.3 The remote sensing detectability of fine mode dust

505

The FM part of the KLRS and DV PSDs clearly covary with their CM analogue (see the PSDs in the Supplementary material, S7). This suggests a weak but robust presence of FM dust. While FM dust is likely a relatively minor optical component (especially at the lidar wavelength), its transport dynamics would likely differ from CM dust, and it could add to the long-distance spread of local dust in the Arctic. Figure 10 is a temporal plot of the 500 nm τ_f and τ_c AERONET product, as well the FM-integrated OPS particle-volume concentration ($v_f(0)$) on the D_{RS} (POI 7-1 and POI 7-2) day of May 7, 2019²².

²² The limitation of τ_c to 500 nm applies only to this specific case: otherwise τ_c is computed at the lidar wavelength of 1.548 μm in the rest of the paper

510 Significant correlation of low and high frequency can be observed between τ_f and τ_c and between τ_f and $\nu_f(0)$. It should be noted that one expects a significant τ_f background (bottoming out) in the Arctic (see AboEl-Fetouh et al., 2020 for example) and this would tend to disrupt the dust-based correlation with τ_c and with $\nu_f(0)$ prior to the beginning of the dust event (around 19:20 UTC). This suggests that a satellite-based, AOD remote sensing technique at a few visible and near IR wavelengths (the equivalent of what is employed by AERONET to extract τ_f and τ_c at 500 nm) would have a reasonable chance of extracting a

515 τ_f dust component and thus contribute to the type of spatial information that one could aspire to extract from satellite-based remote sensing (one can, specifically aspire to extract the MODIS fine mode fraction product of $\tau_f/(\tau_f + \tau_c)$ that can then be converted to a τ_f estimate)

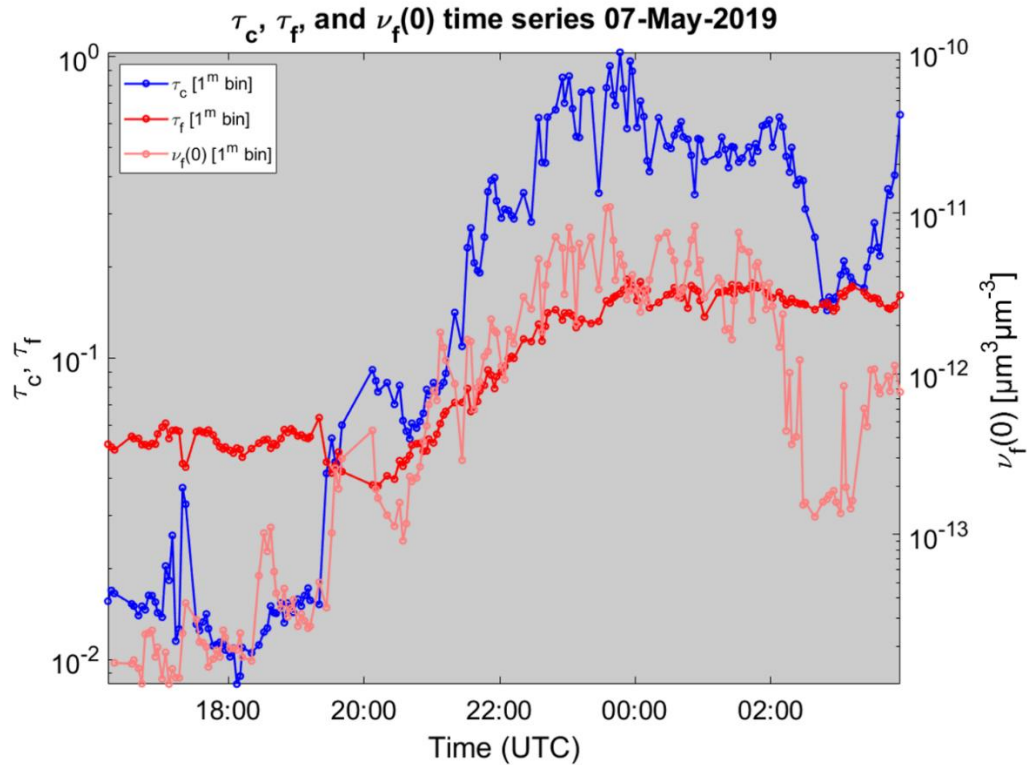


Figure 10: Temporal plot of τ_f and τ_c (500 nm) retrievals along with KLRs OPS surface particle-volume FM concentration $\nu_f(0)$ on May 7, 2019. The $\nu_f(0)$ data has been resampled to the 1 minute ("1^m") AERONET bins (with intersample times of 3 minutes).

5 Conclusions

We reported on an automated dust classification scheme for which the first steps were the derivation of the dust plume height followed by the definition of a class of optically significant (class "D") dust events. This higher-level classification scheme employed short-wave infrared (1.548 μm) lidar profiles (that were predominantly sensitive to coarse mode (CM)

525 particles) coupled with surface-based microphysical measurements of CM particle-volume concentration. We defined two class- D subclasses (D_{RS} and D_{NRS}) as well as two complementary subclasses (D_{GEN} and D_{FPC}): these represented, respectively, events that could be remotely sensed from a passive ground-based (AERONET-type) spectral AOD sensor (and thus, for example, could likely be remotely sensed by a passive satellite sensor), dust events that could likely not be remotely sensed (NRS), dust events that were identified using data other than OPS data (and/or qualitative evidence such as RGB satellite
530 images) and events that could not be remotely sensed because they were classified as clouds and thus eliminated from analytical consideration by the AERONET cloud screening protocol. We also defined an unclassified (U) class: a U_{RS} sub-class represented events whose surface-based CM particle-volume concentration measurements were speculated to be excessively influenced by local dust dynamics (i.e. not in the same dynamics scale as the remotely sensed (columnar) dust optical depths). The associated lack of dust sensitivity was estimated to have an upper limit threshold to be roughly in the
535 10^{-11} – 10^{-10} $\mu\text{m}^3\mu\text{m}^{-3}$ range corresponding respectively to a CM optical depth of 0.001 to 0.1.

The average OPS effective radius of class- D events as measured at the KLRS site (near the CIMEL and lidar instruments) during the month of May 2019 was estimated to be 2.26 ± 0.23 μm . A value of dust refractive index at the lidar wavelength was estimated as $1.5371(\pm 0.0028) - 0.00075(\pm 0.00072) i$ from an analysis Lhù'àn Mân' dust speciation classes. A prescribed lidar ratio of 10.7 ± 0.9 sr was derived from Mie computations employing the OPS-derived effective radius average
540 and the computed refractive index information as input. The CIMEL-derived lidar ratio showed a positive bias that was anywhere from two to three times the prescribed ratio depending on QA constraints placed upon the statistical data employed for its derivation. The persistence of this positive bias led to a hypothesis that the prescribed value could be increased to the CIMEL-derived values of 20 sr by hypothesizing the presence of optically significant dust particles at an effective radius of ~ 11 – 12 μm . This large-particle hypothesis is not incoherent with OPS measurements (such a particle size is greater than its 4.5
545 μm upper limit) and is coherent with the fact that the AERONET PSD retrievals showed a CM whose peak radius increased with increasing dust optical depth.

AERONET inversions were few and far between (and generally weak in terms of τ_c amplitude during the whole month of May 2019). The available inversions showed bimodal CM PSDs with (AERONET bin-center) peaks at radii ~ 1.3 μm and 5.0–6.6 μm and a tendency to be progressively more dominated by the latter peak as $\tau_{c,inv}$ increased. Those larger $\tau_{c,inv}$ values
550 generally occurred during D_{RS} events. The smaller 1.3 μm radius peak was, we argued, likely to be the ubiquitous CM peak that AboEl-Fetouh et al. (2020) ascribed to springtime Asian dust. The latter 5.0–6.6 μm peak is arguably associated with local Lhù'àn Mân' dust peak represented by a broad 2.0–4.5 μm peak in the KLRS OPS data (but, arguably, of lesser effective radius because of the 4.5 μm (bin-center) cutoff of the OPS PSDs).

Finally, we discussed the possibility of extracting a FM dust component using satellite-based remote sensing. This could
555 yield a unique spatial perspective on the opto-physical dynamics of FM dust: a component that is not well understood (see, for example, Cottle et al., 2013) but that might well play an important role in the spread of dust around the Arctic. Moving beyond

the relatively coarse spatial resolution of the workhorse MODIS sensor, both the CM and FM AOD dust products could be derived for high spatial resolution satellites such as those of the PlanetScope constellation.

6 Appendices

560 Appendix A1. Theoretical background for S_c^p validation

Let S_c^p be the current prescribed (constant) value of the dust lidar ratio that was employed to compute τ_c^ℓ ($\tau_c^\ell = S_c^p \tau_{\beta c}$)²³.

The AERONET derived value (S_c) for the D_{RS} class would then be:

$$S_c = \frac{\tau_c}{\tau_{\beta c}} = \frac{\tau_c \tau_c^\ell}{\tau_c^\ell \tau_{\beta c}} = \frac{\tau_c}{\tau_c^\ell} S_c^p \quad (\text{A1})$$

If we are employing $\log \tau_c^\ell$ vs $\log \tau_c$ regressions over the POI then²⁴;

$$565 \quad \log \tau_{c,reg}^\ell = a \log \tau_c + b \text{ where } a \text{ and } b \text{ are the regression slope and intercept. Accordingly;} \quad (\text{A2a})$$

$$\frac{\tau_{c,reg}^\ell}{\tau_c} = 10^b \tau_c^{a-1} \quad (\text{A2b})$$

Employing equation (A2b) in the “reg” version of equation (A1) yields;

$$S_{c,reg} = \frac{\tau_c}{\tau_{c,reg}^\ell} S_c^p = S_c^p 10^{-b} \tau_c^{1-a} \quad (\text{A2c})$$

This corresponds to a situation where a given data pair, (τ_c, τ_c^ℓ) is forced to lie on the regression line (i.e. equation (A2a)) is employed to compute the point $(\tau_c, \tau_{c,reg}^\ell)$. An objective and pragmatic quality indicator of the lidar ratio would be the lidar ratio residuals (“subscript “r”) given by;

$$\Delta S_{c,r} = S_c - S_{c,reg} = \frac{\tau_c}{\tau_c^\ell} S_c^p - \frac{\tau_c}{\tau_{c,reg}^\ell} S_c^p = \tau_c S_c^p \left(\frac{1}{\tau_c^\ell} - \frac{1}{\tau_{c,reg}^\ell} \right) \quad (\text{A3})$$

where S_c is the S_c of Eq. (A1) and where one would compute the average ($\langle \Delta S_{c,r} \rangle$) and standard deviation ($\sigma(\Delta S_{c,r})$) over each POI. In practice, there are large variations in $\Delta S_{c,r}$ and attendant large variations of S_c . Weights defined as $\omega =$
 575 $100 \times 1/(\Delta S_{c,r})^2$ are an indicator of confidence in a given S_c value which places considerably more confidence on (τ_c, τ_c^ℓ) points that are close to the regression line (the weighting factor is inspired by the classical standard deviation weighting factors;

²³ Note that we have deliberately avoided using the D_{RS} classification symbol to minimize the complexity of the equations.

²⁴ In the absence of instrumental or environmental artifacts τ_c and τ_c^ℓ should be governed by Eq. (A1) for a given POI (i.e. assuming S_c doesn’t change during that POI). Accordingly;

$$\log \tau_c^\ell = \log \tau_c + \log \frac{S_c^p}{S_c} = \log \tau_c + b_0$$

which is the analogue of Eq. (A2a) with $a = 1$. Inserting this expression into equation (A1) yields $S_c = S_c^p 10^{-b_0}$. Accordingly, in the absence of instrumental or environmental artifacts, an (Eq. (A2a)) regression slope of, $a \rightarrow 1$ and $R_{log} \rightarrow 1$ should yield better estimates of S_c .

see, for example, Taylor, 1997). The weighted means and standard deviation over a given D_{RS} event would be then computed as;

$$\langle S_c \rangle_\omega = \frac{\sum \omega S_c}{\sum \omega} \quad (\text{A4a})$$

$$580 \quad \sigma_\omega(S_c) = \sqrt{\frac{\sum \omega \Delta S_{c,\omega}^2}{\sum \omega}} \quad (\text{A4b})$$

where we define $\Delta S_{c,\omega} = S_c - \langle S_c \rangle_\omega$. The $\mathbf{1}/(\Delta S_{c,r})^2$ weighting can produce excessively non-linear weights for single measurements very near the (τ_c, τ_c^l) regression line. However, their impact is considerably dampened out because we average over the POIs and then average those averages over the month.

Appendix A2. Processing-related notes of AERONET AODs

585 A2.1 SDA and SDA⁺ retrievals:

The SDA and SDA⁺ retrievals are defined in O'Neill et al. (2003) and O'Neill et al. (2008), respectively. The SDA⁺ input wavelengths are 380 nm, 440 nm, 500 nm, 675 nm, 870 nm, 1020 nm, and 1640 nm. For the purposes of comparing AERONET data with the KLRS Doppler lidar, the SDA⁺ output wavelength was taken as 1548 nm.

A2.2 Backscatter Coefficient (β_c) profiles:

590 The lidar profiles begin at a nominal altitude of 13 m. The minimum reliable measured range is <100 m (typically 75 m) (Newsom & Krishnamurthy, 2020). Our investigation into the KLRS lidar measurements shows that column measurements <51 m often appear to be artifactual (abnormally large and discontinuous $\beta_c T^2$ values as in the case of May 1). Hence, we chose to assign NaN to $\beta_c T^2$ values in this altitude range (notably to eliminate their contribution to τ_{dust}^l).

Appendix A3. Measurements bins and intersample times: (i) native and (ii) common-bin configuration

595 To match the measurement times of all the ground-based CIMEL, lidar and OPS instruments at the KLRS site, we employed the nominal CIMEL times (i.e. the centers of the 1^m CIMEL triplet bins) to generate a linear interpolation of lidar optical depths at their nominal times (the center of their 11 second time bins) and of OPS CM volume densities at their nominal times (center of their 1 minute time bins) to the nominal CIMEL times.

A3.1 CIMEL timing protocols

600 The CIMEL timing protocols, which are the basis for the τ_c time bins (actually any AERONET AOD time bin to be precise) can be found in Giles et al. (2019). Accordingly, a triplet AERONET measurement is performed every 3 minutes to separate homogeneously dispersed aerosols from highly temporally variable clouds. This is effected through a filtering process that measures triplet variability. As stated by Giles et al. (2019), a triplet is a “*series of measurements of all filters starting at 0 s*

of the minute for a duration of about 8 s, and then repeating this measurement sequence at 30 s and 60 s from the initial
605 measurement time. The resulting 1 min averaged measurement [1 min average of the digital number for each filter of the 3
sets of the 8 s measurements] sequence is defined as a triplet measurement and the maximum to minimum range of these
measurements [between individual filter measurements of the 8 s sets] is termed the triplet variability... . The triplet
measurements are performed every 3 min for newer CE318-T instruments ”

7 Author contribution

610 **Seyed Ali Sayedain:** Writing – original draft preparation – review & editing, Visualization, Investigation, Conceptualization,
Methodology, Formal analysis, Data curation, Validation, Software. **Norm T. O’Neill:** Writing – review & editing,
Supervision, Visualization, Conceptualization, Methodology, Formal analysis, Data curation, Validation, Funding acquisition,
Resources. **James King:** Writing – review & editing, Supervision, Data curation, Funding acquisition, Resources. **Patrick L.
615 Hayes:** Writing – review & editing, Data curation, Resources. **Daniel Bellamy:** Writing – review & editing, Data curation,
Validation. **Richard Washington:** Writing – review & editing, Data curation, Resources. **Sebastian Engelstaedter:** Writing
– review & editing, Data curation, Resources. **Andy Vicente-Luis:** Writing – review & editing, Validation. **Jill Bachelder:**
Validation. **Malo Bernhard:** Validation.

8 Competing interests

The authors declare that they have no conflict of interest.

620 9 Acknowledgements

Financial support was provided by the Canadian Mountain Network (CMN) and the Discovery Grant program of the
Canadian National Sciences and Engineering Research Council (NSERC). Valuable in-kind support was provided respectively
by the AEROCAN network of Environment and Climate Change Canada (ECCC) and the NASA AERONET network.
Valuable AERONET processing advice was provided by Tom Eck and Sasha Smirnov of the AERONET team.

625 10 Acronym and symbol glossary

In this glossary we employ, for the sake of simplicity, an argument of “(z)” to represent “(0,z)” for transmission (T)
expressions and no argument for optical depth parameters when their columnar extent is made evident by their subscript

AEROCAN Canadian subnetwork of AERONET

AERONET Aerosol Robotic Network of CIMEL sunphotometer / sky radiometers

$\beta'(z)$	Attenuated backscatter coefficient ($\beta(z) T_c^2(z)$ with units of $\text{km}^{-1} \text{sr}^{-1}$)
AOD	Aerosol Optical Depth (unitless)
$\beta'(z)$	Attenuated backscatter coefficient ($\beta(z) T_c^2(z)$ with units of $\text{km}^{-1} \text{sr}^{-1}$)
$\beta_c(z)$	Coarse mode backscatter coefficient (units of $\text{km}^{-1} \text{sr}^{-1}$)
$\beta'_c(z)$	Coarse mode attenuated backscatter coefficient ($\beta_c(z) T_c^2(z)$ with units of $\text{km}^{-1} \text{sr}^{-1}$)
$\beta_{c,-}(z)$	β_c approximation given by equation (2)
CM	Coarse Mode (generally super-micron radius; see O'Neill et al., 2023 for a general discussion of microphysical and optical considerations)
D	Classification symbol for optically significant dust event
D_{FPC}	“ D ” subclass symbol for an FPC event
D_{GEN}	“ D ” subclass symbol for dust that has been identified using alternate (“generic”) information
D_{NRS}	“ D ” subclass symbol for optically significant dust that cannot be remotely sensed
D_{RS}	“ D ” subclass symbol for optically significant dust that can be remotely sensed
DLH	Dust layer height (units of km)
DV	Down valley
$dv/d\log D$	Particle-volume distribution ($\mu\text{m}^3\mu\text{m}^{-3}$ per unit increment in log diameter). This PSD is derived from the particle number PSD output of the OPS instruments ($dn/d\log D$ where dn is the particle number in a given size bin). Note that $\frac{dv}{d\log r} = \frac{dv}{d\log D}$
$dv/d\ln r$	Particle-volume distribution ($\mu\text{m}^3\mu\text{m}^{-3}$ per unit increment in $\ln r$). Note that $dv/d\ln r = \frac{dv}{d\log r} \frac{1}{\ln 10}$
$dV/d\ln r$	Columnar particle-volume per unit area in the differential bin $d\ln r$ (this is an AERONET inversion product (units of $\mu\text{m}^3\mu\text{m}^{-2}$)
FPC	Subclass subscript acronym for a dust-induced false positive cloud event
FM	Fine Mode (generally submicron radius; see O'Neill et al., 2023 for a general discussion of microphysical and optical considerations)
HLD	High Latitude Dust
KLRS	Kluane Lake (Lhù'ààn Mân') Research Site
LCH	Lidar Ceiling Height (9.6 km)
MCA	Minimum cloud altitude (units of km)
NaN	Not a number
OPC	Optical Particle Counter (from which $v_{dust}(0)$ is determined)
OPS	Optical Particle Sizer (from which $v_{dust}(0)$ is determined)
POI	Period of Interest
PSD	Particle Size Distribution
r	Radius (μm)

R_{log}	Correlation coefficient in log-log space ($\log \tau_c^\ell$ vs $\log \tau_c$ for example)
SDA	Spectral Deconvolution Algorithm
S_c	AERONET derived lidar ratio
S_c^p	Prescribed lidar ratio computed from Mie calculation using surface measured estimates of dust-particle effective radius and refractive index
$S_{c,reg}$	AERONET derived lidar ratio where we force a given data pair, $(\tau_c, \tau_{dust}^\ell)$ to lie on the regression line (subclass D_{RS} data pairs: the “c” subscript is used to simplify the nomenclature)
$\sigma(x)$	Arithmetic standard deviation of the parameter x
$T_c(z)$	Altitude dependent (one-way) transmission of a lidar pulse
$T_{c,-}(z)$	$T_c(z)$ approximation obtained by employing the ratio $\tau_{\beta'_c}(0, z)/\tau_{\beta'_c}^\ell$ as the altitude defining profile of $\tau_c(0, z)$
τ_{β_c}	Column-integrated CM backscatter coefficient (coarse mode backscatter optical depth)
$\tau_{\beta'_c}$	Column-integrated CM attenuated backscatter coefficient (CM attenuated backscatter optical depth)
τ_c	CM AOD at 1548 nm (AERONET SDA ⁺ product)
$\tau_{c,inv}$	CM AOD at 1548 nm (extrapolation of the 4-band AERONET-inversion product)
τ_c^ℓ	CM lidar AOD at 1548 nm with integrating range of 0 – LCH
$\tau_{D,reg}^\ell$	CM lidar AOD at 1548 nm where we force a given data pair, (τ_c, τ_D^ℓ) to lie on the regression line
τ_{dust}^ℓ	CM lidar AOD at 1548 nm with integrating range of 0–DLH ($\tau_c^\ell(0, DLH)$)
τ_D^ℓ	Sequence of τ_{dust}^ℓ values that are promoted to a class D POI
τ_{cloud}^ℓ	CM lidar AOD at 1548 nm with integrating range of DLH–LCH (cloud region)
U	Classification acronym for events that failed to achieve a D classification
$v_{dust}(0)$	Surface ($z = 0$) CM OPS particle-volume concentration at KLRS (units of $\mu\text{m}^3\mu\text{m}^{-3}$). The CM OPS integration was computed over 9 bins whose bin-center radii ranged from 0.78 to 4.51 μm
V_c	AERONET-derived, CM columnar particle-volume concentration (units of $\mu\text{m}^3\mu\text{m}^{-2}$). The CM integration of the $dV/dlnr$ retrieval is computed from the bin containing the $dV/dlnr$ minimum (that dynamic minimum being constrained to a bin-center radius range from 0.439 to 0.992 μm) to the largest retrieval bin (15 μm bin-center radius)
$\langle x \rangle$	Arithmetic mean of the parameter x
z	Altitude above ground level (units of km)

References

- 630 AboEl-Fetouh, Y., O'Neill, N. T., Ranjbar, K., Hesarak, S., Abboud, I., and Sobolewski, P. S.: Climatological-Scale Analysis of Intensive and Semi-intensive Aerosol Parameters Derived From AERONET Retrievals Over the Arctic, *Journal of Geophysical Research: Atmospheres*, 125(10), doi:[10.1029/2019jd031569](https://doi.org/10.1029/2019jd031569), 2020.

- Bachelder, J., Cadieux, M., Liu-Kang, C., Lambert, P., Filoche, A., Galhardi, J. A., Hadioui, M., Chaput, A., Bastien-Thibault, M. P., Wilkinson, K. J., King, J., & Hayes, P. L.: Chemical and microphysical properties of wind-blown dust near an actively retreating glacier in Yukon, Canada, *Aerosol Science and Technology*, 54(1), 2–20, doi:
635 [10.1080/02786826.2019.1676394](https://doi.org/10.1080/02786826.2019.1676394), 2020.
- Baldo, C., Formenti, P., Nowak, S., Chevaillier, S., Cazaunau, M., Pangui, E., Di Biagio, C., Doussin, J. F., Ignatyev, K., Dagsson-Waldhauserova, P., Arnalds, O., Mackenzie, A. R., & Shi, Z.: Distinct chemical and mineralogical composition of Icelandic dust compared to northern African and Asian dust. *Atmospheric Chemistry and Physics*, 20(21), 13521–13539, doi:[10.5194/acp-20-13521-2020](https://doi.org/10.5194/acp-20-13521-2020), 2020.
- 640 Bullard, J. E., Matthew, B., Tom, B., John, C., Eleanor, D., Diego, G., Santiago, G., Gudrun, G., Richard, H., Robert, M., Cheryl, M.-N., Tom, M., Helena, S., & Thorsteinsson, T.: High latitude dust in the Earth system *Reviews of Geophysics*, *Reviews of Geophysics*, 54, 447–485, doi:[10.1002/2016RG000518](https://doi.org/10.1002/2016RG000518), 2016.
- Chiang, C.-W., Nee, J.-B., & Chen, W.-N.: Lidar ratio and depolarization ratio for cirrus clouds, *Applied Optics*, Vol. 41, Issue 30, Pp. 6470–6476, 41(30), 6470–6476, doi:[10.1364/AO.41.006470](https://doi.org/10.1364/AO.41.006470), 2002.
- 645 Cottle, P., Strawbridge, K., Mckendry, I., O'Neill, N., & Saha, A.: A pervasive and persistent Asian dust event over North America during spring 2010: Lidar and sunphotometer observations, *Atmospheric Chemistry and Physics*, 13(9), 4515–4527, doi:[10.5194/acp-13-4515-2013](https://doi.org/10.5194/acp-13-4515-2013), 2013.
- Crusius, J., Schroth, A. W., Gassó, S., Moy, C. M., Levy, R. C., & Gatica, M.: Glacial flour dust storms in the Gulf of Alaska: Hydrologic and meteorological controls and their importance as a source of bioavailable iron, *Geophysical Research Letters*, 38(6), 1–5, doi:[10.1029/2010GL046573](https://doi.org/10.1029/2010GL046573), 2011.
- 650 Dagsson-Waldhauserova, P., Renard, J. B., Olafsson, H., Vignelles, D., Berthet, G., Verdier, N., & Duverger, V.: Vertical distribution of aerosols in dust storms during the Arctic winter, *Scientific Reports*, 9(1), 1–11, doi:[10.1038/s41598-019-51764-y](https://doi.org/10.1038/s41598-019-51764-y), 2019.
- Dörnbrack, A., Stachlewska, I. S., Ritter, C., & Neuber, R.: Aerosol distribution around Svalbard during intense easterly
655 winds, *Atmospheric Chemistry and Physics*, 10(4), 1473–1490, doi:[10.5194/ACP-10-1473-2010](https://doi.org/10.5194/ACP-10-1473-2010), 2010.
- Dubovik, O., & King, M. D.: A flexible inversion algorithm for retrieval of aerosol optical properties from Sun and sky radiance measurements, *Journal of Geophysical Research Atmospheres*, 105(D16), 20673–20696, doi:[10.1029/2000JD900282](https://doi.org/10.1029/2000JD900282), 2000.
- Esselborn, M., Wirth, M., Fix, A., Weinzierl, B., Rasp, K., Tesche, M., & Petzold, A.: Spatial distribution and optical
660 properties of Saharan dust observed by airborne high spectral resolution lidar during SAMUM 2006. *Tellus, Series B: Chemical and Physical Meteorology*, 61(1), 131–143, <https://doi.org/10.1111/j.1600-0889.2008.00394.x>, 2009.
- Evan, A., Walkowiak, B., & Frouin, R.: On the Misclassification of Dust as Cloud at an AERONET site in the Sonoran Desert, *Journal of Atmospheric and Oceanic Technology*, 1(aop), doi:[10.1175/JTECH-D-21-0114.1](https://doi.org/10.1175/JTECH-D-21-0114.1), 2021.
- Evans, B., personal communication, 1994.

- 665 Formenti, P., Caquineau, S., Desboeufs, K., Klaver, A., Chevaillier, S., Journet, E., and Rajot, J. L.: Mapping the physicochemical properties of mineral dust in western Africa: mineralogical composition, *Atmos. Chem. Phys.*, 14, 10663–10686, <https://doi.org/10.5194/acp-14-10663-2014>, 2014.
- Giles, D. M., Sinyuk, A., Sorokin, M. G., Schafer, J. S., Smirnov, A., Slutsker, I., Eck, T. F., Holben, B. N., Lewis, J. R., Campbell, J. R., Welton, E. J., Korkin, S. V., & Lyapustin, A. I.: Advancements in the Aerosol Robotic Network (AERONET) Version 3 database - Automated near-real-time quality control algorithm with improved cloud screening for Sun photometer aerosol optical depth (AOD) measurements, *Atmospheric Measurement Techniques*, 12(1), 169–209, doi:[10.5194/amt-12-169-2019](https://doi.org/10.5194/amt-12-169-2019), 2019.
- Groot Zwaaftink, C. D., Grythe, H., Skov, H., & Stohl, A.: Substantial contribution of northern high-latitude sources to mineral dust in the Arctic, *Journal of Geophysical Research*, 121(22), 13,678–13,697, doi:[10.1002/2016JD025482](https://doi.org/10.1002/2016JD025482), 2016.
- 675 Hesaraki, S., O’Neill, N. T., Lesins, G., Saha, A., Martin, R. V., Fioletov, V. E., Baibakov, K., & Abboud, I.: Comparisons of a Chemical Transport Model with a Four-Year (April to September) Analysis of Fine- and Coarse-Mode Aerosol Optical Depth Retrievals Over the Canadian Arctic, *Atmosphere - Ocean*, 55(4–5), 213–229, doi:[10.1080/07055900.2017.1356263](https://doi.org/10.1080/07055900.2017.1356263), 2017.
- Hansen, J.E., Travis, L.D.: Light scattering in planetary atmospheres, *Space Sci Rev* **16**, 527–610, <https://doi.org/10.1007/BF00168069>, 1974.
- 680 Holben, B. N., Eck, T. F., Slutsker, I., Tanré, D., Buis, J. P., Setzer, A., Vermote, E., Reagan, J. A., Kaufman, Y. J., Nakajima, T., Lavenu, F., Jankowiak, I., & Smirnov, A.: AERONET - A federated instrument network and data archive for aerosol characterization, *Remote Sensing of Environment*, 66(1), 1–16, [https://doi.org/10.1016/S0034-4257\(98\)00031-5](https://doi.org/10.1016/S0034-4257(98)00031-5), 1998.
- 685 Huck, R. A., Bryant, R. G., and King, J.: The importance of detection thresholds for the quantification of source and timing of high-latitude dust emission using remote sensing, *EGUsphere* [preprint], <https://doi.org/10.5194/egusphere-2022-1156>, 2023.
- Kawai, K., Matsui, H., & Tobo, Y.: Dominant Role of Arctic Dust With High Ice Nucleating Ability in the Arctic Lower Troposphere, *Geophysical Research Letters*, 50(8), 1–10. <https://doi.org/10.1029/2022GL102470>, 2023.
- 690 King, J.: X-ray Diffraction determined mineralogy and complex refractive indices of PM10 from the A’ay Chu. Unpublished manuscript, 2023.
- Meinander, O., Dagsson-Waldhauserova, P., Amosov, P., Aseyeva, E., Atkins, C., Baklanov, A., Baldo, C., Barr, S. L., Barzycka, B., Benning, L. G., Cvetkovic, B., Enchilik, P., Frolov, D., Gassó, S., Kandler, K., Kasimov, N., Kavan, J., King, J., Koroleva, T., Krupskaya, V., Kulmala, M., Kusiak, M., Lappalainen, H. K., Laska, M., Lasne, J., Lewandowski, M., Luks, B., McQuaid, J. B., Moroni, B., Murray, B., Möhler, O., Nawrot, A., Nickovic, S., O’Neill, N. T., Pejanovic, G., Popovicheva, O., Ranjbar, K., Romanias, M., Samonova, O., Sanchex-Marroquin, A., Schepanski, K., Semenov, I., Sharapova, A., Shevnina, E., Shi, Z., Sofiev, M., Thevenet, F., Thorsteinsson, T., Timofeev, M., Silas Umo, N., Uppstu, A., Urupina, D.,

- Varga, G., Werner, T., Arnalds, O., Vukovic Vimic, A.: Newly identified climatically and environmentally significant high-latitude dust sources. *Atmospheric Chemistry and Physics*, 22(17), 11889–11930, <https://doi.org/10.5194/acp-22-11889-2022>, 2022.
- 700 Newsom, R., & Krishnamurthy, R.: Doppler Lidar (DL) Instrument Handbook, doi:[10.2172/1034640](https://doi.org/10.2172/1034640), 2020.
- Nickling, W. G.: Eolian Sediment Transport During Dust Storms: Slims River Valley, Yukon Territory, *Can J Earth Sci*, 15(7), 1069–1084, doi:[10.1139/e78-114](https://doi.org/10.1139/e78-114), 1978.
- O'Neill, N. T., Eck, T. F., Reid, J. S., Smirnov, A., & Pancrati, O.: Coarse mode optical information retrievable using ultraviolet to short-wave infrared Sun photometry: Application to United Arab Emirates Unified Aerosol Experiment data, *Journal of Geophysical Research Atmospheres*, 113(5), 1–11, doi:[10.1029/2007JD009052](https://doi.org/10.1029/2007JD009052), 2008.
- 705 O'Neill, N. T., Eck, T. F., Smirnov, A., Holben, B. N., & Thulasiraman, S.: Spectral discrimination of coarse and fine mode optical depth, *Journal of Geophysical Research D: Atmospheres*, 108(17), 1–15, doi:[10.1029/2002jd002975](https://doi.org/10.1029/2002jd002975), 2003.
- O'Neill, N. T., Ignatov, A., Holben, B. N., & Eck, T. F.: The lognormal distribution as a reference for reporting aerosol optical depth statistics; Empirical tests using multi-year, multi-site AERONET sunphotometer data, *Geophysical Research Letters*, 27(20), 3333–3336, doi:[10.1029/2000GL011581](https://doi.org/10.1029/2000GL011581), 2000.
- 710 O'Neill, N. T., Ranjbar, K., Ivanescu, L., Eck, T. F., Reid, J. S., Giles, D., Perez Ramirez, D., Chaubey, J.: Relationship between the sub-micron Fraction (SMF) and fine mode fraction (FMF) : case of AERONET retrievals, *AMT*, in press, March, 2023.
- 715 Pearson, G., Davies, F., & Collier, C.: An analysis of the performance of the UFAM pulsed Doppler lidar for observing the boundary layer, *Journal of Atmospheric and Oceanic Technology*, 26(2), 240–250, doi:[10.1175/2008JTECHA1128.1](https://doi.org/10.1175/2008JTECHA1128.1), 2009.
- Ranjbar, K., O'Neill, N. T., Ivanescu, L., King, J., & Hayes, P. L.: Remote sensing of a high-Arctic, local dust event over Lake Hazen (Ellesmere Island, Nunavut, Canada), *Atmospheric Environment*, 246, 118102, <https://doi.org/10.1016/j.atmosenv.2020.118102>, 2021.
- 720 Rozwadowska, A., Zieliński, T., Petelski, T., & Sobolewski, P.: Cluster analysis of the impact of air back-trajectories on aerosol optical properties at Hornsund, Spitsbergen, *Atmospheric Chemistry and Physics*, 10(3), 877–893. <https://doi.org/10.5194/acp-10-877-2010>, 2010.
- Sayer, A. M., & Knobelspiesse, K. D.: How should we aggregate data? Methods accounting for the numerical distributions, with an assessment of aerosol optical depth, *Atmos. Chem. Phys*, 19, 15023–15048, doi:[10.5194/acp-19-15023-2019](https://doi.org/10.5194/acp-19-15023-2019), 2019.
- 725 Shugar, D. H., Clague, J. J., Best, J. L., Schoof, C., Willis, M. J., Copland, L., & Roe, G. H.: River piracy and drainage basin reorganization led by climate-driven glacier retreat, *Nature Geoscience*, 10(5), 370–375, doi:[10.1038/ngeo2932](https://doi.org/10.1038/ngeo2932), 2017.
- Sinyuk, A., Holben, B. N., Eck, T. F., Giles, D. M., Slutsker, I., Korkin, S., Schafer, J. S., Smirnov, A., Sorokin, M., & Lyapustin, A.: The AERONET Version 3 aerosol retrieval algorithm, associated uncertainties and comparisons to Version 2, *Atmos. Meas. Tech*, 13, 3375–3411, doi:[10.5194/amt-13-3375-2020](https://doi.org/10.5194/amt-13-3375-2020), 2020.
- 730

Sokolik, I. N., & Toon, O. B.: Incorporation of mineralogical composition into models of the radiative properties of mineral aerosol from UV to IR wavelengths, *Journal of Geophysical Research Atmospheres*, 104(D8), 9423–9444, doi:[10.1029/1998JD200048](https://doi.org/10.1029/1998JD200048), 1999.

735 Taylor, J. R.: An introduction to error analysis : the study of uncertainties in physical measurements, University Science Books, 327pp., 1997.

Weinzierl, B., Petzold, A., Esselborn, M., Wirth, M., Rasp, K., Kandler, K., Schütz, L., Koepke, P., & Fiebig, M.: Airborne measurements of dust layer properties, particle size distribution and mixing state of Saharan dust during SAMUM 2006. *Tellus, Series B: Chemical and Physical Meteorology*, 61(1), 96–117, <https://doi.org/10.1111/j.1600-0889.2008.00392.x>, 2009.

740 Weitkamp, C.: Lidar : range-resolved optical remote sensing of the atmosphere, In Springer series in optical sciences, (Issue 102), doi:[10.1007/b106786](https://doi.org/10.1007/b106786), 2005.

Yang, S., Preißler, J., Wiegner, M., von Löwis, S., Petersen, G. N., Parks, M. M., & Finger, D. C.: Monitoring dust events using doppler lidar and ceilometer in Iceland, *Atmosphere*, 11(12), 1–23. <https://doi.org/10.3390/atmos11121294>, 2020.